Spatiotemporal resonance in mouse primary visual cortex

Rasa Gulbinaite[1], Mojtaba Nazari[2], Michael E. Rule[3], Edgar J. Bermudez-Contreras[2], Michael X Cohen[4], J. Alexander Heimel[1], Majid H. Mohajerani[2]

[1] Netherlands Institute for Neuroscience, Amsterdam, The Netherlands

[2] Canadian Centre for Behavioral Neuroscience, University of Lethbridge, Lethbridge, Canada

[3] Engineering Department, University of Cambridge, Cambridge, United Kingdom

[4] Sincxpress Education SRL, Romania

Corresponding author: rasa.gulbinaite@gmail.com

Number of pages: 42

Number of figures: 5

Number of words: 6882

SUMMARY

Human primary visual cortex (V1) is entrained by the rhythmic light and responds more strongly, or resonates, to ~10, ~15-20, ~40-50 Hz flicker. Full-field flicker also elicits geometric hallucinations, the origin of which has only been explored in computational models and human EEG with limited spatial resolution. Here, we recorded cortical responses to flicker in awake mice using high spatial resolution widefield imaging in combination with high temporal resolution glutamate-sensing fluorescent reporter (iGluSnFR). Resonance frequencies in mouse V1 were similar to those in humans (8 Hz, 15 Hz, 33 Hz). Spatially, all flicker frequencies evoked responses in V1 corresponding to retinotopic stimulus location and some evoked additional spatial peaks. These flicker-induced cortical patterns displayed standing wave characteristics and matched linear wave equation solutions in an area restricted to the visual cortex. Taken together, the interaction of travelling waves with cortical area boundaries leads to spatiotemporal activity patterns, which may affect perception.

INTRODUCTION

Sensory neurons of many species – from fruit flies, rodents, salamanders to humans – stimulated with rhythmic sounds, lights, or touch closely follow the rhythm. This is reflected by the peaks in power spectra corresponding to the stimulus frequency and its harmonics in electroencephalogram (EEG), local field potentials (LFPs), and single unit recordings [1–6]. Aside from this general stimulus frequency-following neural response, a few notable response nonlinearities exist. Foremost, not all input frequencies are processed alike. In human EEG recordings, stronger amplitude responses, or *resonance*, over occipitoparietal areas have been consistently reported for ~10, 15-20, and 40-50 Hz visual rhythmic stimulation [7–9]. Relatedly, phase of steady-state visual evoked potentials (ssVEPs) at resonance frequencies is more stable[9,10], and has been interpreted as entrainment of endogenous brain oscillators operating in the same frequency range [11]. Resonance peaks were also observed in the temporal frequency tuning curves in the cat visual cortex[4].

Temporal frequency tuning curves derived from multiunit and spiking activity in the mouse primary visual cortex (V1) show only a single peak (~6 Hz), with a linear decrease of response amplitude as the flicker frequency increases[12,13]. Studies using voltage-sensitive fluorescent protein (VSFP) imaging – a high temporal resolution mesoscale neural population activity measure – also point to the conclusion that mouse V1 behaves as a low-pass filter[1]. Limited and coarse sampling of temporal stimulation frequencies might have concealed the existence of resonance frequencies in mice and precluded a direct comparison of temporal frequency tuning in human and mouse V1. Direct cross-species comparison, however, holds translational relevance in using the mouse as a model to understand neurophysiological mechanisms underlying normal and abnormal steady-state responses in humans[14], and due to promising therapeutic effects of gamma-band flicker in Alzheimer disease mouse model[15,16].

In addition to amplitude variations in response to different flicker frequencies, human fMRI studies also showed spatial organization of temporal frequency preference across V1[17,18], and V2[19]. In mice and other species, however, there is no evidence for temporal frequency maps[20]. Alternatively, the apparent temporal frequency preference across V1 and V2 found in humans could reflect standing-wave patterns resulting from an interaction between intrinsic cortical oscillations and travelling waves periodically generated in response to repetitive visual stimulation[21,22]. Relatedly, in computational models standing wave formations have been put forward to explain the emergence of flicker-induced hallucinatory visual patterns[23,24]. Although

both standing and travelling waves have been reported in flicker stimulation paradigms in humans[25,26], limited spatial resolution of EEG and cortical gyrification, where a static source could appear as a traveling wave in scalp projections [27,28], makes it difficult to address spatial propagation and spatial distribution of responses to different temporal input frequencies in humans[26,29].

Here, we investigated spatiotemporal propagation of responses to visual flicker in mice using high spatial resolution widefield imaging and fast genetically encoded glutamate sensor iGluSnFR[30]. To directly compare temporal frequency tuning in human and mouse V1, we used a protocol similar to that of Gulbinaite et al.[9] and stimulated with a wide range of flicker frequencies (2-72 Hz). We found that temporal tuning curves in mice showed resonance peaks at 5 Hz, 8 Hz, 15 Hz, and 33 Hz. We also observed that all temporal frequencies elicited responses in V1 corresponding to the stimulus location, yet certain (higher) flicker frequencies elicited responses beyond retinotopic stimulus location. Moreover, spatial frequency of response patterns in V1 increased with flicker frequency. Using spatiotemporal analyses of stimulus-evoked travelling waves (spatiotemporal pattern separation[31], phase latency method[32]), we found that spatial inhomogeneities in responses to flicker observed in power and phase maps are standing waves formed within a nearly circular region corresponding to the borders of the visual cortex. Finally, we demonstrated that flicker-induced cortical patterns matched linear wave equation solutions – the first eigenmodes of discrete Laplace operator in an area restricted to the visual cortex.

RESULTS

Using chronic awake widefield imaging we recorded fluorescence changes of genetically encoded glutamate sensor iGluSnFR expressed in excitatory neurons across all cortical layers in Emx-CaMKII-Ai85 mice[33,34]. To elicit steady-state visual evoked potentials (ssVEPs), we used sine-wave modulated luminance changes (flicker) in a range of finely sampled temporal frequencies (2 to 72 Hz, 30 logarithmically spaced). Each flicker stimulus (10 s) was followed by a long (10 s) inter-stimulus interval to allow fluorescent signal to return to baseline, because a slow neurovascular coupling related hemodynamic signal starting around 1 s post-stimulus and lasting for 4-5 seconds was superimposed on stimulus-related changes in iGluSnFR fluorescence (Figure 1D,E). To remove fluorescence changes related to haemodynamic response, breathing and heartbeat [1,33,35], we applied global signal regression (GSR). GSR correction alone left intact a slow BOLD-like neurovascular response superimposed on evoked responses, which we corrected by

applying a robust detrending procedure[35,36] (Figure 1 D,E). Apart from sine-wave modulated luminance changes, we also recorded evoked responses to visual pulses (20 ms), and brief (1 ms) auditory, hindlimb, forelimb, and whisker stimuli (Figure 1C, Supplementary Figure 1). These sensory event-related potentials (ERPs) were used to create functional maps for each animal and verify alignment of the recording window to Allen Mouse Brain Common Coordinate Framework[36] (Allen CCF; Figure 1C).

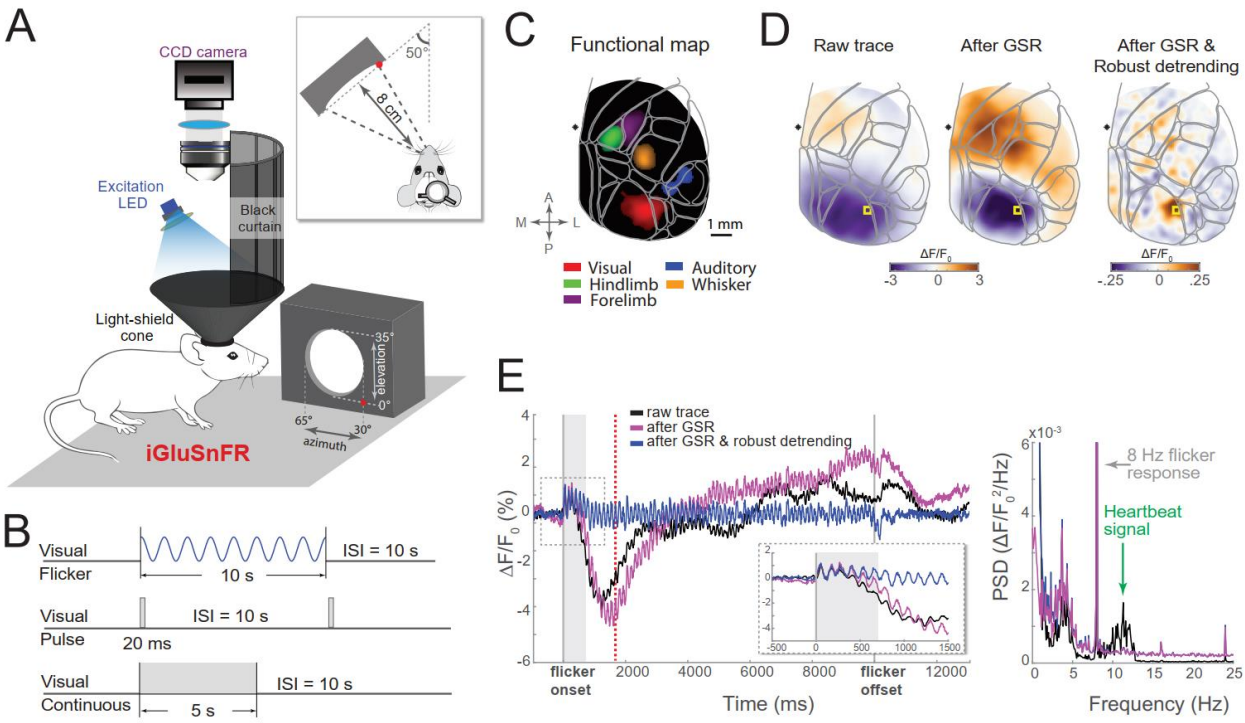

Figure 1. Imaging and stimulation setup, experimental design, and image spatial co-registration to Allen CCF. (A) Schematic drawing of the experimental setup and visual stimulation device. Optical parts (CCD camera, optical lenses, emission filter, excitation LED with excitation filter), light-shielding cone and black curtain to prevent visual stimulation light leaks into the imaging window (see also Supplementary Figure 2). (B) Visual stimulation protocols: Sine-wave modulated luminance changes, single pulse stimuli, and continuous light stimuli. In all paradigms, inter-stimulus interval (ISI) was 10 s long to allow glutamate fluorescence signal to return to baseline. (C) Functional cortical map from a single animal representing an overlay of peak evoked activity (thresholded at 5 SD relative to the baseline). Responses to different sensory stimuli are color coded (red - visual; blue - auditory; orange - whiskers, green - hindlimb, purple - forelimb). Sensory stimulation recordings were co-registered to Allen CCF (light grey outlines). Note a high correspondence between anatomical areas in Allen CCF (VISp, AUDp, SSp-ll, SSp-up, SSp-bfd) and activation peaks in response to different sensory stimulation protocols. (D) Cortical activity maps from the timepoint marked by the red dashed line in panel E. Both raw trace (baseline-corrected $\Delta F/F_0$ fluorescence signal) and GSR-corrected signal show apparent suppression of the entire VISp, whereas signal separation using robust detrending reveals a to-be-expected VISp activation in response to visual stimulation (rightmost cortical map). (E) Left: Baseline-corrected $\Delta F/F_0$ fluorescence signal (1 animal, average of 10 trials, 8 Hz flicker stimulation; black trace) contaminated by heartbeat pulses (green arrow in the power

spectrum on the right) and slow neurovascular coupling related hemodynamics starting ~1 s after the flicker onset, which was attenuated using global signal regression (GSR; pink trace) and robust detrending respectively (blue trace). Inset: Zoomed-in plot from a dotted-line square in the main figure. Grey area (0-700 ms relative to flicker onset) indicates a portion of the ssVEP signal on which robust detrending procedure was not applied to avoid removal of neural signal. All time courses show a clear periodic response to 8 Hz flicker. Right: Power spectrum of three signals depicted on the left, with a steep slope at low frequencies (neurovascular coupling) and strong heart-beat related oscillations (black trace), which are removed by robust detrending and GSR.

Temporal frequency tuning in mouse and human V1 exhibits high degree of similarity

To derive temporal frequency tuning curves from iGluSnFR fluorescence dynamics in the mouse V1, we computed power spectra in response to different flicker frequencies at each pixel and expressed it in SNR units: A ratio between power at the flicker frequency and the weighted sum of power at the neighboring frequencies[14]. Conversion of raw power spectra into SNR units allowed us to account for 1/f power-law scaling effect (power decrease as a function of frequency)[37], and to compare different frequency ssVEP amplitude directly (Supplementary Figure 3).

As expected given the retinotopic organization of the visual cortex, left-hemifield flickering stimulus elicited retinotopically localized response over the right V1 (Figure 2A). No activity in the visual cortex was detected when iGluSnFR was not directly excited by the blue LED light (Supplementary Figure 2). Power spectra from V1 pixels most responsive to the flicker showed a strong peak at the stimulus frequency (1*f*; Figure 2A,C). Conversion of ssVEP power into SNR units also revealed harmonic (up to 5*f*) and subharmonic responses, which were indiscernible in the raw power spectra due to strong 1/f power-scaling effect (Figure 2A vs. 2B). Statistically significant ssVEPs were elicited up to 56 Hz for 1*f* and 66 Hz for 2*f* responses (Figure 2D for 1*f*; Supplementary Figure 4 for 2*f*). Complementing ROI-based analysis, statistical significance of responses up to 56 Hz flicker was also confirmed at the cortical map level (Figure 2E). High temporal resolution of iGluSnFR hallmarked by neural responses up to 66 Hz observed here in chronic *in vivo* recordings matched those reported *in vitro* in hippocampal slice preparations[30] ($\tau_{1/2}$ = 15±11 ms; 1/15*1000 = 67 Hz), and allowed us to track responses to gamma band flicker stimuli.

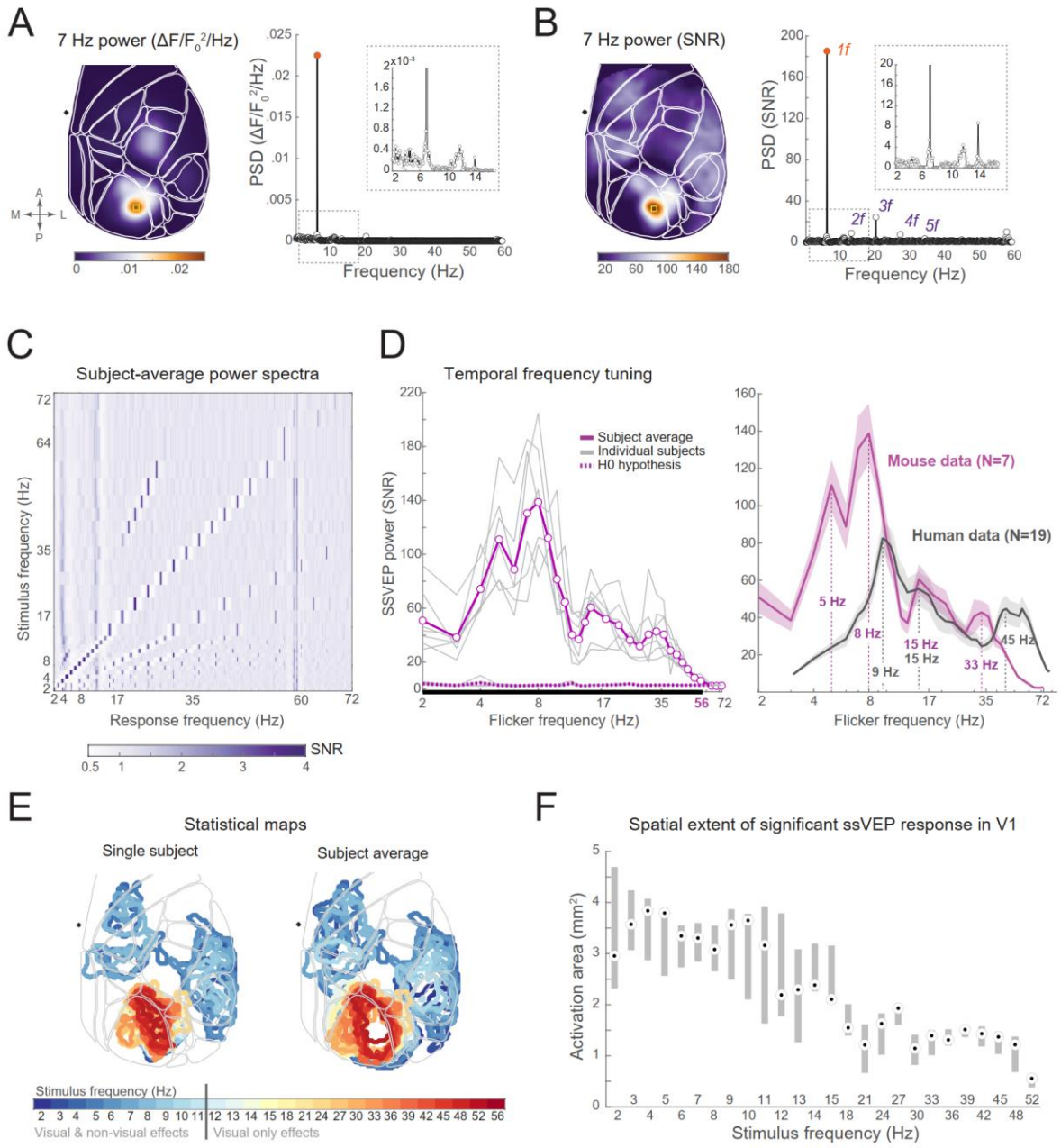

Figure 2. Temporal frequency tuning in mouse visual cortex. (A) Exemplar topography and power spectrum in response to 7 Hz flicker (averaged from 9 pixels around the spatial response peak). Single subject data. (B) Same as A, except power spectrum is expressed in SNR units (power at each frequency expressed relative to the neighboring frequencies in the power spectrum). Insets: Zoomed in plot of the power spectra around the stimulation frequency. Note the appearance of harmonic responses when power spectrum was expressed in SNR units. Yellow squares on the topographical maps indicate maximum power pixels from which the average power spectra were computed. (C) Subject-average power spectra (x-axis) expressed in SNR units plotted as a function of stimulus flicker frequency (y-axis). Note the frequency-following response along the diagonal, as well as harmonic (2*f*, 3*f*, etc.) and subharmonic (1:2) responses. Across all flicker conditions, there was increased power at: (1) 3-5 Hz, which is typically observed in visual stimulation protocols (see the main text); (2) 11-13 Hz, which reflects residual heartbeat artifact; (3) ~57 Hz, which is noise related to CCD camera. (D) Left panel: ssVEP power at all 30 flicker frequencies used

in the experiment, plotted separately for each animal (grey lines) and averaged across animals (N=7, magenta line). Dotted magenta line on the bottom represents ssVEP power on 95th percentile of trials, during which neither flicker frequency nor harmonically related frequencies were presented (the null hypothesis). Statistically significant responses to flicker were observed up to 56 Hz stimulation frequency: The observed ssVEP power was higher than null hypothesis H0 (black thick line on the x-axis). Right panel: Comparison of temporal frequency tuning curves in mice (N=7) and humans (N=19; Gulbinaite et al., 2019). Shaded areas represent standard error of mean. (E) Spatial extent of statistically significant responses as a function of flicker frequency. Color lines enclose contiguous pixels at which power was significantly higher on trials with flicker of interest vs. trials from two neighboring flicker frequency conditions (bootstrap-t procedure; cluster-level correction $p < .01$). All flicker frequencies below 56 Hz elicited statistically significant responses in the visual areas. Additionally, flicker frequencies below 11 Hz elicited responses beyond visual areas (auditory and somatosensory areas). (F) Spatial extent of responses to flicker only in V1 as a function of stimulation frequency (median across animals, grey shaded areas represent 25th and 75th percentiles).

Although response amplitude decreased as flicker frequency increased, ssVEP amplitude decrease was not monotonic: Grand-average temporal frequency tuning curves contained resonance peaks in response to theta (M = 7.57 Hz; SD = 0.53 Hz), beta (M = 16.71 Hz, SD = 2.93 Hz), and gamma (M = 33.86 Hz, SD = 3.34 Hz) band flicker (Figure 2D). Resonance peaks differed across animals, especially in the gamma band (peaks ranged between 30 and 39 Hz). Because mouse heart rate spans 8-14 Hz range[35], by computing temporal frequency tuning curves from visual and non-visual ROIs placed over the blood vessels we verified that resonance peaks were not the result of a heart-beat artifact (Supplementary Figure 7A). Only the visual ROI did contain resonance peaks (Supplementary Figure 7B). Taken together, temporal frequency tuning curves in mice displayed a banded structure, with resonance frequencies highly similar to those previously reported in humans (Figure 2D).

In addition to 3 resonance peaks observed in humans, a fourth ~5 Hz peak in the theta band was also present in mice (M = 4.86 Hz, SD = 0.38; Figure 2D). Endogenous 3-5 Hz oscillations in mouse V1 have been reported in LFPs and single-cell recordings, with the strongest power in layer 2/3[38,39]. The 3-5 Hz rhythm was also prominent in iGluSnFR signal recorded here (Figure 1E; Supplementary Figure 8). Topographically, 3-5 Hz rhythm was constrained mostly to visual areas (Supplementary Figure 8A), was stronger during low (< 20 Hz) vs. high frequency flicker trials (Supplementary Figure 8C), and was not sustained during the trial (Supplementary Figure 8D). Based on the previous reports[38,39], 3-5 Hz rhythm is predominantly observed after the movement, during low arousal states, and after stimulus offset. Here, 3-5 Hz rhythm behaved in the opposite way: It was more prominent during flickering stimulus vs. inter-trial interval and was also stronger during low frequency flicker trials (Supplementary Figure 8 B,C). We speculate that increase in 3-

5 Hz rhythm observed here is related to enhanced breathing, which has been suggested to be the origin of fear-related 4 Hz oscillations[40]. The remaining resonance peaks were exclusively related to the processing of visual stimuli. Time-frequency analyses of responses to pulse and continuous luminance stimuli showed increase in theta (peak M_{pulse} = 6.97 Hz; $M_{ON\text{-}OFF}$ = 7.72 Hz), beta (M_{pulse} = 15.19 Hz; $M_{ON\text{-}OFF}$ = 15.94 Hz), and gamma power (M_{pulse} = 36.1 Hz; $M_{ON\text{-}OFF}$ = 39.84 Hz; Supplementary Figure 6).

Spatiotemporal resonance: Responses beyond retinotopic stimulus location

We next analyzed the spatial distribution of responses to different flicker frequencies by making use of the high spatial resolution of widefield imaging data (67 μm per pixel in our setup) and smooth-brain mouse cortex. To evaluate and compare the spatial extent of responses across different flicker frequencies, t-value maps were computed by comparing cortical maps at a flicker frequency of interest ("signal" map) with cortical maps at that same flicker frequency derived from the two adjacent conditions when a given flicker frequency was not present ("noise" map).

All flicker frequencies up to 56 Hz evoked statistically significant responses in the visual cortex, and lower as compared to higher flicker frequencies elicited responses in larger portions of V1 (N = 7; $F(1,25) = 11.08$, $p < 0.001$; Figure 2F). Additionally, flicker frequencies below 11 Hz elicited responses beyond visual areas (auditory and somatosensory areas; Figure 2E). Further inspection of statistical ssVEP maps revealed spatial response inhomogeneities. While all stimulation frequencies elicited responses at retinotopic location of V1 corresponding to the stimulus position and response amplitude decreased with distance from directly stimulated area, additional spatial peaks were present within V1 in response to some flicker frequencies (Figure 3A and 3B). This variability and non-uniformity of spatial responses could result from structural anisotropies in anatomical connectivity across mouse V1, or from the interaction between locally generated cortical oscillations and a propagating wave generated in response to different frequency rhythmic stimuli. To test the second hypothesis, we performed a guided spatiotemporal pattern analysis using a two-stage generalized eigenvalue decomposition (GED) and isolated the dominant spatiotemporal response features specific to each flicker frequency (see Methods section and Supplementary Figure 9 for an overview of the method).

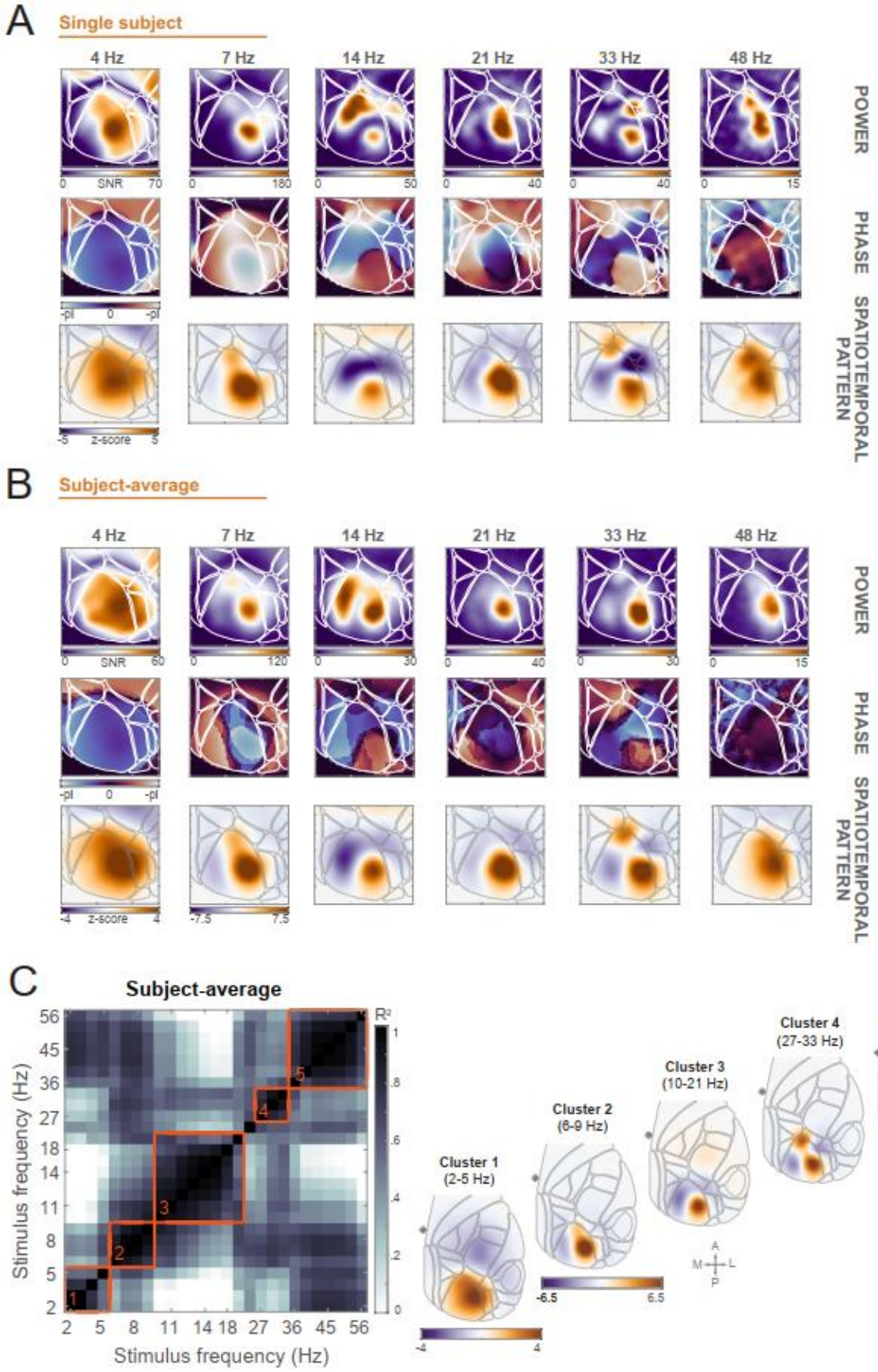
A
Single subject
4 Hz
7 Hz
14 Hz
21 Hz
33 Hz
48 Hz
POWER
PHASE
SPATIOTEMPORAL PATTERN
SNR
z-score
B
Subject-average
C
Subject-average
Stimulus frequency (Hz)
R²
Cluster 1 (2-5 Hz)
Cluster 2 (6-9 Hz)
Cluster 3 (10-21 Hz)
Cluster 4 (27-33 Hz)
Cluster 5 (36-56 Hz)

Figure 3. Spatiotemporal resonance in mouse primary visual cortex. (A) Several exemplar flicker frequency-specific ssVEP power maps, phase maps and spatiotemporal patterns from a single subject. Note that some spatial peaks in ssVEP power maps correspond to different phases in phase maps and spatiotemporal patterns (e.g. cortical maps in response to 14 Hz and 33 Hz flicker). (B) The same as A, but averaged across animals (N=7). Note the high consistency between single animal and subject-average ssVEP maps. (C) Left: Subject-average pairwise squared correlation matrix across spatiotemporal patterns. Characteristic spatial response topographies (five numbered clusters) marked in orange along the diagonal in the correlation matrix were identified using hierarchical clustering procedure.

Spatiotemporal response patterns specific to each flicker frequency were computed separately for each animal and then averaged across animals (Figure 3B). Despite previously reported substantial mouse-to-mouse variability in V1 size[41], we observed a remarkable similarity between single animal and a group-average spatiotemporal patterns evoked by different flicker frequencies. Visual comparison of ssVEP power maps and spatiotemporal patterns revealed that certain secondary spatial peaks in power maps aligned with negative pixel weights in spatiotemporal patterns (e.g. responses to 14 Hz and 33 Hz flicker in Figure 3A,B). The positive and negative peaks indicate opposite phases of stimulus-evoked wave at those locations in V1 and is characteristic to standing wave. Thus, positive and negative peaks correspond to anti-nodes of the standing wave, and region in between represents wave nodes. In phase maps, the wave node region coincided with phase reversals (Figure 3A,B).

To identify similarities across cortical maps elicited by different flicker frequencies, we computed pairwise correlations between frequency-specific spatiotemporal patterns and performed hierarchical clustering on these correlation matrices. Pattern clustering was performed on individual animal and group average correlation matrices. On the group level, five characteristic ssVEP cortical maps were isolated, spatial complexity and number of spatial peaks in which increased with flicker frequency (Figure 3C; e.g. 8 Hz – single spatial peak, 14 Hz – two spatial peaks, 30 Hz – 3 spatial peaks). Per animal, the number of clusters on average was 5.29 (SD = 0.76). Thus, overall the same five characteristic spatiotemporal maps were present in all except one animal (4 maps) and, in some cases, a single group-level cluster was split into two clusters at the animal level (3 animals; Supplementary figure 10).

Travelling and standing waves in mouse V1

Abrupt π radian phase changes (phase reversals) separating large regions of a constant phase prominent in some ssVEP phase maps are characteristic of standing waves (e.g. 7 Hz, 14 Hz, 33

Hz in Figure 3A). The zero amplitude contours roughly corresponding to the borders of the visual cortex suggest that these standing waves could result from reflection of travelling waves at the boundary of visual cortex. Area boundaries here are conceptualized as changes in connectivity and/or signal transmission properties. Previous studies have demonstrated that visual stimuli elicit lateral spreading waves across V1[32,42–44], with some reporting wave deceleration at and reflection from V1 border[45]. Therefore, we next analyzed travelling wave dynamics and standing wave formation.

To investigate wave propagation before standing wave patterns emerged, we analyzed responses to single pulse stimuli (pulse ERP). The spatiotemporal dynamics of pulse ERP highly resembled that of the first cycle low-frequency ssVEPs (Figure 4A). A stimulus-evoked wave propagated anterior and laterally from retinotopic stimulus location within primary visual cortex and gradually spread to medial and lateral visual cortices (Figure 4A; Movie 1 and 2). The first ERP peak at the retinotopic stimulus location (M_{peak} = 50.5 ms; SD_{peak} = 5.2 ms) was followed by a widespread suppression across V1 (M_{trough} = 138.1 ms, SD_{peak} = 10 ms) and a second ERP peak (late component) reappeared at the retinotopic stimulus location (M_{peak} = 219 ms; SD = 13.0 ms; Figure 4B and Supplementary Figure 11). Although there was no observable difference in ERP peak time at different V1 locations, waveform rise time was more delayed at more distant locations relative to peak ROI, indicating an active wave propagation. This contrasted with the falling phase of the ERP waveform, which occurred almost simultaneously in all locations, indicating a spatially coherent suppression.

To quantify the properties of the stimulus-evoked travelling wave, at each pixel we extracted the instantaneous phase from a band-passed filtered (5-25 Hz) ERP waveform, and constructed a phase latency map by computing phase latency differences relative to the timeframe immediately prior to the first ERP peak[32]. Phase latency gradually increased with distance starting from the wave source (minimum of the phase latency map; Figure 4C), as expected from a travelling wave behavior[21,43]. The relationship between phase latency and cortical distance was fairly linear at short distances (within 1000 μm radius from the wave source; see inset in Figure 4C), although the line density in phase latency maps suggested slowing of the propagation speed near the visual cortex border (Figure 4C). We computed wave propagation speed along different directions from the slope of a linear fit to the phase latency and cortical distance relationship. The

average speed propagation across all directions was 0.21 m/s (SD = 0.15 m/s; M_{slow} = 0.11 m/s; M_{fast} = 0.62 m/s; Figure 4D).

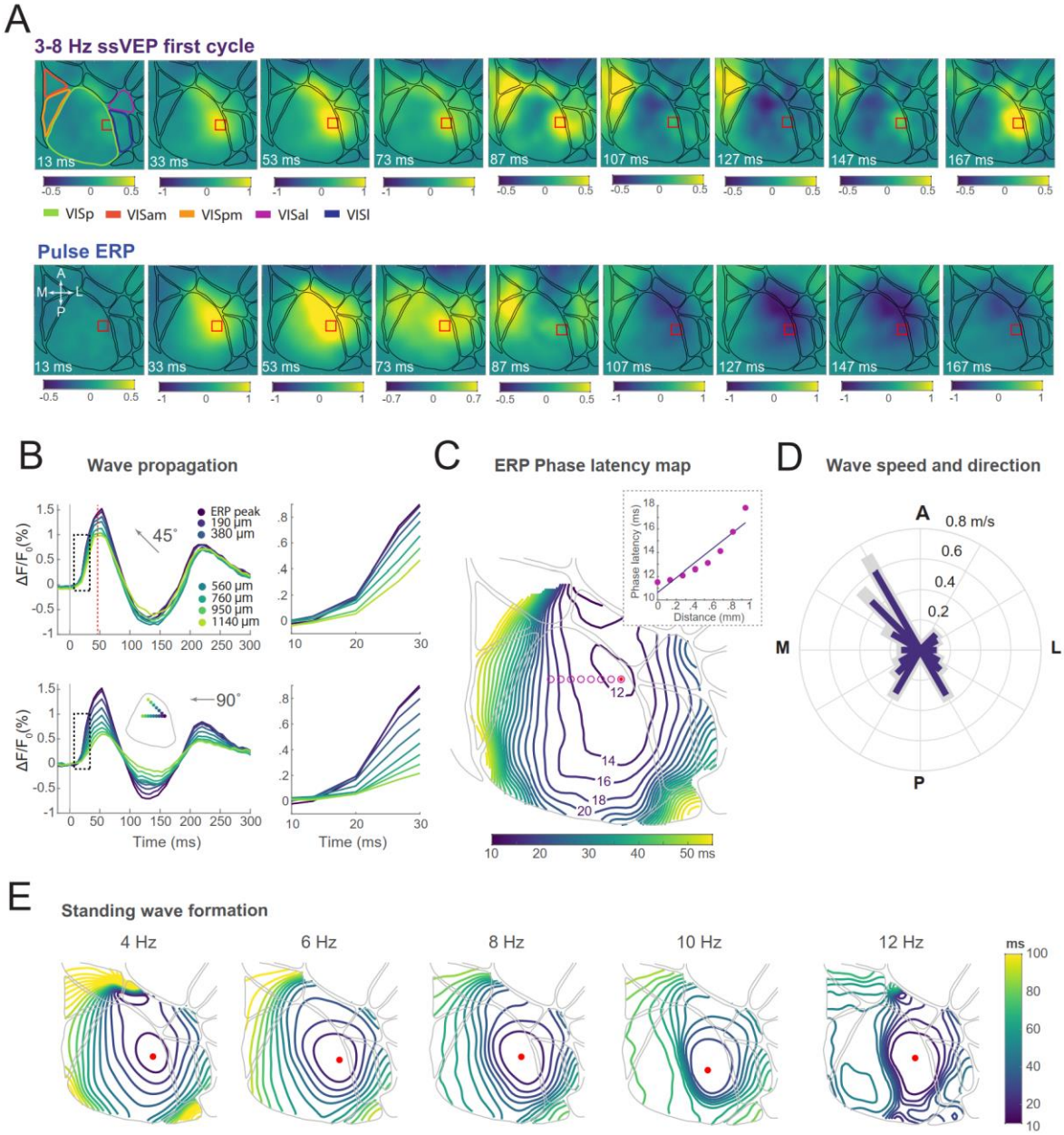

Figure 4. Travelling and standing waves in mouse visual cortex. (A) Time-lapse images of stimulus-evoked activity during the first cycle of 3-8 Hz sine-wave stimulation (averaged across conditions; top row) and pulse ERP (bottom row). Red rectangle indicates spatial location of the first ERP peak. Note the lateral spread of activity within the primary visual cortex (VISp), and a later spread to lateral (VISl) and medial visual areas (VISam, VISpm). Data from a single animal. (B) Left panels: ERP waveforms from different locations along the two directions starting from the first ERP peak ROI (45 and 90 degrees counterclockwise relative to A-P axis), with cortical distance also expressed relative to the first ERP peak ROI. Right panels: Zoomed in version of the left-side plots indicating delayed rise time as the distance from the peak ERP pixel increases. Higher amplitudes along the 45 degree direction indicate active and faster wave

propagation. (C) Phase latency map of pulse ERP. The map is calculated +47 ms after the stimulus onset (reference timepoint), such that the represented phase latency map depicts phase relation over space at the time of the first ERP peak. The red dot marks the minimum of the phase latency map (source of the wave) and isocontour lines depict phase offset (in milliseconds) relative to the reference timepoint. (D) Distribution of wave propagation velocity along different directions averaged across animals (blue bars). Grey areas indicate Mean + SEM. Velocity along some directions could not be estimated for all the animals (non-monotonically increasing phase at VISp borders) and thus is not depicted. (E) Phase latency maps of different ssVEPs. Note the progressive phase increase across space at low flicker frequencies (4-6 Hz) and abrupt phase changes, indicative of a standing wave, at higher flicker frequencies (12 Hz). Phase latency maps were calculated from peak-triggered average ssVEP waveforms. Exemplar data from a single animal.

While a single flash elicits a single propagating wave, continuous rhythmic stimulation gives rise to multiple interacting waves, providing the mechanism for the formation of spatial ssVEP response patterns. Thus, we next analyzed the effects of flicker after a steady-state mode of responding has been reached (1000 ms after onset of the flicker). To increase the signal-to-noise ratio, we re-epoched ssVEP data relative to every 5th peak in the stimulus sine-wave and averaged these short epochs. Inspection of phase latency maps constructed from stimulus-peak-triggered averages revealed that with increasing flicker frequency the phase latency maps progressively resembled a standing wave pattern: Gradual phase increase over space at 4 Hz stimulation was replaced by abrupt phase changes at 10-12 Hz stimulation (Figure 4E; Movie 3 and 4).

Spatiotemporal resonance patterns and linear wave equation

Spatiotemporal patterns and phase-latency analysis indicated that cortical patterns in V1 elicited by >5 Hz flicker frequencies exhibit standing wave characteristics (Figure 3 and 4). These standing waves formed within a roughly circular region outlined by the zero amplitude contours observed in ssVEP power maps. Therefore, we explored which standing wave patterns could theoretically be formed within a medium characterized by isotropic connectivity with nearly circular boundaries.

The standing wave solutions to the standard wave equation (see Methods) are eigenmodes of the Laplace operator (∇^2). We used a matrix form of discrete Laplace operator to describe the connections between pixels in the image. We assumed local (only adjacent pixels are connected) and isotropic connectivity within the modelled region, and given the observed small ssVEP amplitude at the borders, we assumed no activity at the boundary (Dirichlet boundary conditions). The modelled region was defined separately for each animal based on amplitude contours in ssVEP maps (Figure 5B and Supplementary Figure 12). We found that the first eigenmodes of discrete

Laplace operator on the modelled region closely resembled the empirically observed spatiotemporal ssVEP patterns (Figure 5A). This finding further supports the interpretation that spatiotemporal ssVEP patterns are standing waves evoked by the rhythmic light stimulation.

Next, we quantified the similarity between the eigenmodes and the empirical spatiotemporal ssVEP patterns (Figure 5C). We found that overall faster temporal frequencies were associated with higher spatial frequency eigenmodes, except for the narrow "one-lobe" eigenmode which was not associated with a specific flicker frequency (Figure 5C). Given that all flicker frequencies elicited a spatially localized response in V1 corresponding to the retinotopic stimulus location, a narrow "one-lobe" eigenmode presence at all flicker frequencies captures this common spatially localized response. Although eigenmodes were not uniquely associated with one specific flicker frequency, a range of flicker frequencies predominantly excited one specific eigenmode.

To determine the relationship between temporal driving frequency and spatial frequency of the evoked standing wave patterns (dispersion relation), we assumed that the waves originating from the source travel at a constant velocity and are attenuated with distance. This wave propagation behavior is described by a damped wave equation, based on which the stimulus temporal frequency f and the eigenmode k together with the associated eigenvalue η_k are square-root related $f = \sqrt{-c^2\eta_k - d^2}$ (c is wave propagation velocity and d the damping term; for details on derivation of dispersion relation, see Methods). To estimate coefficients c and d, we used eigenvalue spectra to identify a range of temporal stimulus frequencies f associated with particular Laplacian eigenvalue η_k and fitted the dispersion relation (black line in Figure 5D). Wave propagation coefficient c on average was 0.087 m/s and corresponded to empirically observed wave propagation speeds (Figure 4D). The damping coefficient d was 164.14 1/s (i.e. τ = 6 ms). The adjusted R^2 of the fitted dispersion relation was 0.74. Note that when $-c^2\eta_k - d^2 < 0$, the standing waves do not form and spatiotemporal responses resemble a low-pass filtered version of the input. Assuming that the observed waves are planar, we derived relationship between the spatial scale of the evoked standing-wave patterns (wavelength λ) and flicker frequency (Figure 5E). Finer spatial response patterns were associated with higher flicker frequencies.

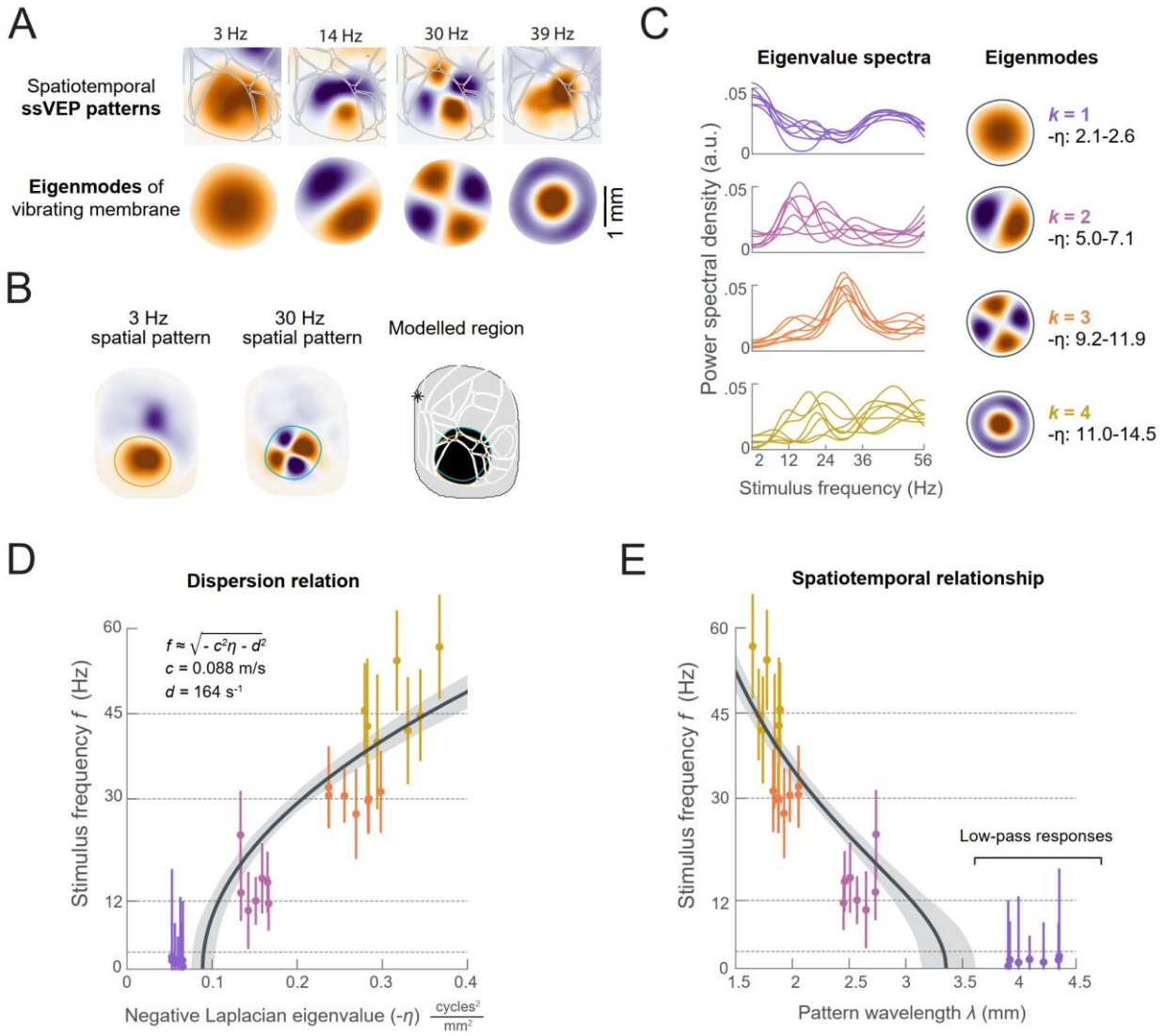

Figure 5. Relationship between spatiotemporal flicker-induced cortical patterns and eigenmodes of vibrating 2D membrane. (A) Visual similarity between the spatiotemporal patterns elicited by different flicker frequencies and standing waves (eigenmodes) of a nearly circular vibrating membrane. (B) The union of regions excited by 3 Hz and 30 Hz flicker was used to define a region of posterior cortex on which standing-wave pattern formation was modelled. (C) Left: Eigenvalue spectra computed as a squared dot product between eigenvectors corresponding to a specific Laplacian eigenmode $k = 1,2,3,4$ and normalized ssVEP maps from different flicker frequencies. Eigenvalue spectra reflect how strongly each Laplacian eigenmode was present in ssVEP maps across different flicker conditions (x-axis). Each line represents data from a single animal. Right: Eigenmodes of a nearly circular modelled region, k is an index of the mode and η_k is the range of Laplacian eigenvalues associated with a particular eigenmode. The actual Laplacian eigenvalue depends on the geometry of the modelled region and thus is different across animals, hence the range. (D) Relationship between temporal stimulus frequency (f) and Laplacian eigenvalues η_k corresponding to specific spatial patterns (eigenmodes) elicited by the flickering stimulus. Color notation is the same as in panel C and indicates different eigenmodes. Each datapoint represents a peak eigenvalue in eigenvalue spectra (panel C), with the spread reflecting FWHM of the peak. Solid black line represents a fitted dispersion relation. (D) Assuming that the observed waves are planar, we derived the relationship between the wavelength λ of the spatial pattern of each eigenmode and the temporal stimulus frequency f (see Methods section for details).

DISCUSSION

Leveraging the high spatial resolution of widefield imaging with the fast kinetics of glutamate fluorescent reporter, we demonstrate that at a population level, mouse V1 responds to and can follow much faster luminance changes than previously reported (56 Hz here, 24 Hz in Andermann et al.[46]). In line with previously documented low-pass filtering characteristics of V1[1,12], response amplitudes gradually decreased as flicker frequency increased, however this decrease was not monotonic: Some flicker frequencies elicited stronger responses (resonance) which appeared as local peaks in the temporal frequency tuning curves. Thus, mouse V1, just like human and cat V1[4,7,9,47], favors some temporal input frequencies. We further found that responses to lateralized flickering stimuli extended far beyond retinotopic stimulus location and were spatially inhomogeneous. By analytical means and modelling we demonstrate that the observed cortical spatial response patterns reflect standing waves resulting from propagation, interference and superposition of stimulus-evoked travelling waves.

V1 low-pass filter settings – not so low after all

Response amplitude in mouse V1 decreases as stimulus temporal frequency increases[1,12,48], and slowly (1.5-3 Hz) drifting gratings, on average, elicit stronger responses[46,48,49]. These findings gave V1 a reputation of a sluggish low-pass filter, although temporal and spatial frequency preference of V1 neurons span a wide range (up to 24 Hz tested Andermann et al.[46]; up to 16 Hz in Han et al.[47]). Such findings, however, do not imply that at a population level, V1 is not capable of following rapidly changing inputs. Using full-field luminance changes, a 6 Hz peak in temporal frequency tuning curves has been reported in multiunit activity and responses to 40 Hz flicker are evident in LFP recordings in mouse V1[13,15]. Here, using widefield imaging of a fast genetically encoded glutamate sensor iGluSnFR expressed in excitatory neurons in all cortical layers we recorded significant responses to luminance changes up to 56 Hz in mouse V1. Temporal resolution of glutamate reporter (iGluSnFR) was not a limiting factor: Responses twice the stimulus frequency were significant up to 66 Hz (i.e. 33 Hz stimulation; Supplementary Figure 4). Thus, widefield imaging, alongside other neural population recording methods (MUA, LFP), revealed a higher temporal resolution of mouse V1. Mouse ability to discriminate high frequency flicker has also been reported behaviorally, with critical flicker fusion frequency, and thus

temporal resolution, in mice reaching 42 Hz[50]. Under what circumstances would such high temporal resolution be necessary? Although static flickering stimuli are unlikely to be encountered in a natural environment, detection of fast moving predators and accurate interception of prey is not only perceptually relevant[51].

Although steady-state visual evoked potential (ssVEP) waveforms primarily contain the stimulus frequency (1*f*), harmonically related frequencies are also present even if stimulus luminance is modulated by a pure sinewave[9]. Harmonic responses are generally assumed to reflect response non-linearities of the visual system[14,52]. In the glutamate signal, harmonic responses were also present, with up to 5*f* peaks (Figure 2A,C). Subharmonic responses *f*/2 (18-26 Hz), corresponding to half the stimulation frequency and thus referred to as period-doubling, were also present in response to gamma-band flicker (36-52 Hz, see Figure 2C). Period doubling, which is retinal ganglion cell response to every other flash, has been recorded in electroretinograms (ERG) of several species (humans, salamanders, rats)[2,53]. In rats, period doubling has been reported to 20-30 Hz input frequencies, whereas in humans, only >30 Hz flicker elicits *f*/2 responses. Thus, subharmonic responses recorded here most likely were also of retinal origin.

V1 temporal resonance and endogenous oscillations

In response to a wide range of flicker frequencies (2-72 Hz), response amplitude non-monotonously decreased as the temporal stimulus frequency increased. After accounting for power-law scaling, we found local maxima (resonance) in temporal frequency tuning curves in response to theta (~5 Hz), alpha (~8 Hz), beta (~15 Hz), and gamma (~33 Hz) flicker. In humans, using the same stimulation paradigm we previously found peaks in alpha, beta, and gamma bands (see Figure 2D). Although the observed resonance peaks in alpha and gamma bands were lower in mice than in humans (7-8 Hz vs. 9-13 Hz range; 30-39 Hz vs. 43-65 Hz) and an additional peak in mice was present in the theta band (~5 Hz), the overall banded structure of temporal frequency tuning suggests that resonance phenomena are preserved across species and hallmark common cortical computations.

In humans, resonant stimulus frequencies match the frequencies of endogenous alpha and gamma oscillation in the visual cortex, determined either from the resting state recordings or stimulus-evoked EEG[9,10,54]. Aside from enhanced amplitudes, responses to resonance flicker frequencies show a stronger phase locking to the stimulus[9,10], and instantaneous response

frequency fluctuates less around the stimulus frequency[9]. What endogenous oscillations are present in mouse V1 and how do they relate to the observed resonance peaks in temporal frequency tuning curves?

In mouse V1 temporal frequency tuning curves, two adjacent resonance peaks were present in the theta band (~5 Hz and ~8 Hz; in rodent literature, 4-10 Hz is considered the theta band), reflecting two different sources of endogenous theta oscillations at play. Based on previous reports, 3-5 Hz rhythm is the most prominent rhythm in awake mouse recordings. It is the strongest in L2/3, increases following movement (whisking or locomotion) and after stimulus offset, and overall it is stronger during low arousal states[38,39]. Dynamics of 3-5 Hz rhythm recorded here, during flicker stimulation, was diametrically opposite: Stronger power during stimulus as compared to inter-trial interval, and enhanced power during slow frequency flicker trials (presumably more arousing context). Given these findings, we hypothesize that increase in 3-5 Hz rhythm and thus resonance peak at ~5 Hz was related to enhanced breathing, especially during low flicker trials (Supplementary Figure 8). Respiration as the origin of ~5 Hz resonance peak is further supported by the findings of ~4 Hz rhythm during fear behavior, with strong modulatory effects of breathing on V1 activity (both LFPs and spikes)[40]. The resonance peak at ~8 Hz, on the other hand, was purely related to visual stimulus processing, as ~8 Hz oscillations were also the most prominent rhythm in response to pulse and on-off continuous stimulation (Supplementary Figure 6), and also have been previously reported[55]. Previous interpretation of 6-9 Hz activity in V1 as volume conduction of hippocampal theta synchronized to visual stimulation is unlikely[38], as imaged signal here was optical rather than electrical, ~8 Hz peak was present during stimulus but not inter-trial interval, and hippocampal theta is not strongly entrained to visual stimulation[16].

Peaks in beta (~15 Hz) and gamma (~33 Hz) in temporal frequency tuning curves observed in glutamate signal were also present in response to single pulse and continuous visual stimulation (Supplementary Figure 6), and matched the frequencies of visually evoked oscillations in LFP recordings reported previously. Visual stimulation elicits gamma (peak 30-40 Hz[56–58]) and weak beta (~15 Hz[55,59]) oscillations in L4 and L2/3, with gamma peak frequency dependent on stimulus properties. We also found substantial inter-subject variability in gamma resonance frequency (peak ranged from 30 to 39 Hz). Given that gamma oscillations are only reliably elicited by the grating stimuli[58,60], whereas only weak gamma responses are observed in response to flash stimuli[57],

steady-state stimulation paradigm we used here might be an alternative and reliable way to elicit gamma oscillations.

Responses to repetitive light stimulation set up standing waves in the visual cortex

When examining the spatial extent of responses to a localized flickering stimulus, we found that in addition to a consistent response in V1 corresponding to the stimulus location, some flicker frequencies also elicited non-retinotopic responses. Using several spatiotemporal analysis methods and simulations of wave propagation within an isotropically connected medium with boundaries, we demonstrate that spatial response variations across visual cortex reflect standing waves, the spatial frequency of which increases with increased temporal driving frequency.

Consistent with previous reports[42,56,61], both single pulse and flicker stimuli evoked travelling waves spreading from retinotopic stimulus location (Figure 4). The wave propagation velocity ranged from 0.1 to 0.6 m/s and is similar to those reported in awake ECoG recordings in mice (0.1-0.8 m/s)[56], VSD recordings in anesthetized cats (0.3 m/s)[43], and awake primates (0.57 m/s)[32]. Such propagation speeds correspond to signal propagation along unmyelinated cortico-cortical horizontal fibers in superficial layers[22]. Although widefield imaging signal is a weighted sum of fluorescence across all cortical layers, the signal mostly comes from superficial layers of the cortex[62]. Similar to previous reports[56,61], we found that stimulus-evoked waves propagated preferentially towards anterior regions, with some bias towards anteromedial directions.

Spatiotemporal response patterns to >5 Hz flicker exhibited characteristics of standing waves within a nearly circular region (Figure 5). In physical systems, standing waves typically form due to wave reflection from the boundaries. Although stimulus-evoked wave reflection from architectonic V1/V2 border has been reported in anesthetized rat recordings[45], boundaries could also be set up by stimulus-related wave interaction. Such temporary boundaries, for example, could be setup by fast spreading inhibition, evidence for which was apparent in response to pulse stimuli (Movie 1; Figure 4A). This fast inhibition is $GABA_A$-mediated and might reflect feedback from higher visual areas, LGN or both[44]. Alternatively, temporal boundaries could also be set up by an interaction between feedforward wave in V1 and feedback waves from higher-order visual areas travelling at different speeds[56,63]. In this scenario, a temporary signal transmission boundary is a result of wave collision and interference[64]. Regardless of the mechanism by which boundaries arise, we found that eigenmodes in an isotropically connected medium with nearly circular

boundaries closely resembled the empirically observed spatiotemporal patterns evoked by locally flickering stimulus. The area within which the standing waves were formed appeared to include V1 and some higher visual areas. Wave propagation beyond V1 was also supported by phase latency analysis and is consistent with the findings in mice[65] and rats[45].

Flicker-induced standing wave patterns observed here could also explain topographical variability in responses to different flicker frequencies reported in human EEG studies[9,26], and apparent spatial organization in temporal frequency tuning across visual hierarchy in fMRI studies [18,19]. Dual-peak responses in EEG could reflect a standing wave, which cannot be resolved due to limits of spatial Nyquist frequency and volume conduction, with only long wavelengths reported in previous flicker stimulation EEG studies[25,26,29]. Based on findings in the mouse visual cortex, spatial response variability in macroscale signals like EEG could result from similar wave propagation and interaction principles reported here.

Cortical wave relation to flicker-induced hallucinatory patterns

In humans, uniformly flickering field induces pseudo-hallucinatory percepts that often take the form of moving concentric circles, spirals, tunnels, fans, lattices, and honeycombs[23]. While the perceived patterns vary with flicker frequency for individual participants, no systematic relationship between the driving frequency and perceived forms has been established across participants[66]. Spatial frequency of flicker-induced percepts, however, seems to increase with increasing temporal stimulation frequency[67]. Already early theories linked flicker-induced percepts to standing wave patterns in the visual cortex elicited by the rhythmic stimuli[68]. The idea was implemented in neural field models using Wilson-Cowan equations[24,69,70]. In these models, a uniform external oscillating input breaks the cortical excitation-inhibition balance and sets up network oscillations, which at certain external stimulation frequencies self-organize into standing waves. Rule and colleagues, for example, have found that standing wave patterns emerge at stimulation frequencies that match or are twice higher than endogenous oscillations of the simulated neural network (resonance frequencies)[24]. Empirical studies in humans also demonstrated that percept formation speed and strength peak when stimulated at resonance frequency of the human visual cortex (~10 Hz)[71,72]. However, so far no studies have demonstrated a direct causal link between flicker-induced percepts and standing waves in neural recordings.

Whether flicker-induced standing wave activity beyond retinotopic stimulus location was perceived by the animal, and whether standing wave patterns recorded here are related to flicker-induced percepts in humans is unclear. The spatial frequency of standing waves in mouse visual cortex was ~1 mm at 30 Hz flicker stimulation, which corresponds to ~40° of visual angle. The spatial scale of geometric hallucinatory percepts in humans is much finer, with estimated size of hallucinatory features spanning 1-2 mm of the human brain surface[23]. Nonetheless, finding positive relationship between standing wave spatial frequency and flicker frequency in mice goes in the same direction as reported relationship between spatial frequency of hallucinations and flicker frequency: Not only hallucinatory patterns appearing at higher flicker frequencies are finer and more detailed, but sudden doubling or halving of the frequency respectively increases or decreases the number of hallucinatory features without altering the pattern[67,68]. Except for these early studies, rigorous tests on temporal frequency dependent spatial scaling of hallucinatory patterns are missing. However, spatial frequency of standing waves could, in principle, account for such relationship between the spatial scale of geometric hallucinatory patterns and temporal driving frequency.

Conclusions

Wide-field imaging using a fast glutamate sensor allowed us to investigate spatiotemporal dynamics in response to repetitive stimulation with high spatial and temporal resolution. In addition to amplification of responses to some input frequencies (resonance), we found spatial inhomogeneities in response to different flicker frequencies across visual cortex. Faster temporal frequencies elicited higher spatial frequency ssVEP patterns: Progressing from a single- to double- to four-peak patterns. We demonstrate that empirically observed cortical spatial response patterns reflect standing waves, which can be approximated by a linear wave equation, with Laplacian eigenmodes bearing high resemblance to empirically observed spatiotemporal response patterns.

MATERIALS AND METHODS

Animals

All experimental procedures were approved by Animal Welfare Committee of the University of Lethbridge and were performed in accordance with guidelines established by the Canadian Council for Animal Care.

Widefield glutamate imaging was performed in seven transgenic adult mice (5-6 month old, 4 females) expressing genetically encoded glutamate sensor iGluSnFR in glutamatergic neocortical neurons (Emx-CaMKII-Ai85 strain). The Emx-CaMKII-Ai85 mice were obtained by crossing the lines Ai85D (Jax026260)[73], Camk2a-tTA (Jax007004)[74], and Emx1-IRES-Cre (Jax005628)[75]. Prior to chronic window surgery, the animals were housed in groups of two to five under standard conditions in clear plastic cages with 12h light and 12h dark cycle. Mice had ad libitum access to water and standard laboratory mouse food. Following the implantation of a chronic imaging window, the animals were housed individually to prevent injuries and damage of the imaging window.

Chronic Imaging Window Surgery

Chronic imaging windows over an intact skull were installed over the right hemisphere in mice (4 female and 3 male) that were 5-6 month old, following previously published procedures[34,76]. The animals were anesthetized with 2.5% isoflurane, with anesthesia maintained with 1-1.5% isoflurane. Throughout the surgery, body temperature was monitored by a rectal thermometer and maintained at 37°C using a feedback-regulated heating pad. Following induction of the general anesthesia, the scalp was locally anesthetized with lidocaine (0.1 ml, 0.2%), after which the fur and the head skin was removed. The skull was cleaned up from fascia and connective tissue, exposing the right side of the skull. Thereafter, the clean and dry skull was covered with a clear version of C&B-Metabond dental cement (Parkell, Inc.) and a metal head-plate was glued using dental cement. Finally, the skull was covered with a glass coverslip. Following awakening from anesthesia, the animals were put in the recovery room for a 24h period, after which they were placed in their home cage and monitored daily. The animals were allowed to recover from the surgery for at least 1 week before habituation to the experimental procedures was started.

Analysis of pilot recordings revealed that despite extensive measures aimed at protecting the imaging area from light exposure of the white LED visual stimulation device (custom-designed

3D printed plastic protection and black non-reflective curtain covering the imaging area, see Figure 1), light leaks through the skin and small openings between the head-plate and the skull were present in the frontal part of the imaging window (Supplementary figure 2). Therefore, 3 weeks after the initial surgery, the animals underwent a short procedure during which an additional layer of black dental cement was applied over the frontal and lateral parts of the head-plate fixation and the skin. This procedure was carried out under general anesthesia, controlling the body temperature and using the antiseptic techniques as previously described. This additional procedure successfully eliminated light artifacts (see Supplementary Figure 2).

Habituation

Following a full recovery from the chronic imaging window implantation surgery, the animals were trained to remain head fixed using a 7-day incremental training time procedure, which minimizes animal stress. The first day, animals were placed on the head fixation setup for 5-10 minutes and were allowed to freely move and explore the setup. On subsequent days, the mice were head-fixed using two clamps for 5 minutes, with increasing time per session (from 5 minutes up to 30 minutes), food reward followed each training session. During habituation and recording, body movement and stress were minimized by putting them in the enrichment plastic tube from their home cage. Sounds and vibrations in the recording setup and the room were minimized, light stimulation was present during the habituation stage to simulate the experimental protocol.

Imaging

In vivo glutamate imaging was performed in awake head-fixed animals using a charge-coupled device (CCD) camera (1M60 Pantera, Dalsa, Waterloo, ON) and an EPIX E8 frame grabber with XCAP 3.8 imaging software (EPIX, Inc., Buffalo Grove, IL). The onset and offset of CCD camera and behavioral camera, onset and offset of each frame, as well as voltage changes corresponding to luminance changes of the visual stimulation device were recorded in Clampex (Molecular Devices, Sunnyvale, CA) and used for data analyses to determine frames during which visual stimulation was delivered. During the imaging, the behavioral camera and an infrared light were placed in front of the animal to constantly monitor active behavior and any signs of distress.

To capture the fast glutamate sensor iGluSnFR kinetics, images of iGluSnFR activity were captured at 150 Hz sampling rate. The glutamate fluorescent indicator was excited using blue LED light (Luxeon K2, 470 nm), which was band-pass filtered using an optical filter (Chroma

Technology Corp, 467-499 nm). Light emitted from excited fluorescent indicators was passed through a band-pass optical filter (Chroma, 510 to 550 nm; Semrock, New York, NY) and a macroscope composed of front-to-front optical lenses. The focal length of the lenses was adjusted such that the field of view was 8.6 × 8.6 mm (128 x 128 pixels, with 67 μm per pixel). To minimize the effect of hemodynamic signal originating from large cortical blood vessels, we focused the optical lens at ~1mm depth.

Visual stimulation setup

We used a custom-built setup of white light-emitting diodes (LEDs; luminous intensity 6900 mcd, color temperature 9000K, Model C513A-WSN, Cree Inc.) to deliver visual stimulation (the setup previously used in Gulbinaite et al.[9]). The LED array was placed in a cardboard box, with a circular aperture subtending 35° of visual angle covered by a sheet of tracing paper (6 cm away from LED array). The visual stimulation box was placed on the left side of the animal, 8 cm from the left eye, at a 50° angle to the animal's body axis. The luminance of white LEDs was linearized using a quadratic function, such that a linear increase in voltage corresponded to a linear increase in luminance (measured in cd/m^2). Flicker was implemented as a sine-wave modulation of the power supply to the LEDs (luminance changes from 0 to 215 cd/m^2), which was controlled using a microcontroller of the STM32F4-Discovery board by adjusting the width of PWM signal and linearizing the current using a low-pass filter. MATLAB was used for communication with the STM32F4-Discovery board via a USB virtual com port protocol (programmed in C++). Voltage changes driving the changes in luminance of stimulation LEDs were recorded in pClamp (Molecular Devices, Sunnyvale, CA) as a separate channel in Axon Binary Files (ABFs). Recorded waveform was used to determine the CCD camera frames during which visual stimulation was delivered.

Stimulation protocols

Steady-state visual evoked potentials. On each trial, the animals were exposed to 10 s of flicker followed by 10 s inter-trial interval of complete darkness (Figure 1C). Mice were exposed to flicker frequencies that ranged from 2 to 72 Hz (logarithmically spaced 30 different frequencies). For all frequencies, the stimulation has started and ended with maximal luminance (215 cd/m^2, pi/2 phase of the sine-wave cycle). Each imaging session lasted up to 30 minutes, during which each flicker frequency was presented twice in pseudo-random order. Each animal underwent 5 experimental

sessions (i.e. 5 recordings on separate days). Thus in total, each flicker frequency was presented 10 times (10 s * 10 = 100 s per frequency), and the recording duration was comparable to that previously used in a human study (96 s per flicker frequency)[9].

After each experimental session, the excitatory blue LED light used to excite the glutamate fluorescent indicator was switched off and 5 Hz flicker was presented for 3 trials (10 s flicker, 10 s inter-trial interval). This control recording was used to determine the presence and the extent of any potential light artifact from the visual stimulation leaking into the imaging window through the skin and/or junction of the 3D printed light-blocking cone and the head-plate (see Figure 1A for the setup; Supplementary figure 2).

Visual evoked-potentials. In addition to sine-wave stimulation, we recorded responses to single light pulses (20 ms) and continuous light stimulation (5 s) using 1500 cd/m^2 luminance stimuli to characterize spatiotemporal dynamics in response to single stimuli and on/off responses.

Sensory evoked-potentials. Stimulation of other senses was performed in anaesthetized animals (1% isoflurane) and was used to determine the coordinates of other primary sensory areas[34,77]: Hindlimb area of primary somatosensory cortex (SSp-ll), forelimb area of the primary somatosensory cortex (SSp-ul), primary barrel sensory cortex (SSp-bfd), and primary auditory cortex (AUDp). The forelimb and hindlimb were stimulated electrically (1 mA, 1 ms electrical pulse) with a thin acupuncture needle inserted into the paws. The C and D whiskers were stimulated using a piezoelectric bending actuator, and a single 1 ms tone (25 kHz) was used for auditory stimulation. Each stimulus was followed by 10 s inter-stimulus interval. Sensory evoked potentials were calculated by averaging 20-30 trials.

Image preprocessing and analysis

Spatial co-registration across recordings and to Allen CCF. Recordings obtained on different days and different animals were co-registered using rigid transformations (translation and rotation). Prior to each recording session, a stack of 15 reference images was taken by focusing the lens around the depth of blood vessels. Reference images were then merged into one image using ImageJ. The transformation matrix used for the alignment across recording sessions was computed as follows. First, the images from each animal's first session were translated (x and y direction) to match bregma (marked during the window-placement surgery) to an arbitrarily chosen reference

point (x=10, y=30), and rotated such that the axis connecting bregma-lambda was parallel to the bregma-lambda axis in the Allen Institute Common Coordinate Framework (CCF) map. Thereafter, reference images from each subsequent session were co-registered to the reference images of the first acquisition using surface vasculature and anatomical landmarks. Hereby obtained transformation matrices were then applied to the image stack of a corresponding recording session. 2D Allen CCF map was obtained from 3D Allen CCF mouse brain rotated 30 degrees counterclockwise around the anterior-posterior axis to accommodate for the tilted (~30 degree) placement of the headplate over the right hemisphere. The quality of alignment to Allen CCF was verified by creating a functional map: Plotting the evoked potentials from all sensory stimulation paradigms (Figure 1F; Supplementary figure 1).

Preprocessing and hemodynamic artifact removal. Continuous recordings were first epoched around the stimulus onset (-2–15 s for ssVEP paradigm, -2–9 s for 5 s continuous visual stimulation, -2–4 s for visual pulse stimulation, -1–1 s for auditory, forelimb, hindlimb and whisker stimulation). Non-brain pixels were masked prior to further signal preprocessing steps. To remove temporal changes in glutamate fluorescence related to hemodynamic response, breathing and heart rate[33], we applied global signal regression (GSR). If we denote fluorescence signal at each pixel *i* and timepoint *t* as $S_i(t)$, the global signal regressed out was a time-average of each pixel:

$$g(i) = \frac{1}{T}\sum_{t=1}^{T} S_i(t)$$

The GSR-corrected signal is then:

$$S_{GSR}(t) = S(t) - g\beta_g(t)$$

where $\beta_g(t) = g^+S(t)$ and g^+ is a pseudo-inverse of g ($g^+ = [g^Tg]^{-1}g^T$). Such signal normalization over time effectively removes hemodynamic artifacts in pixels containing blood vessels and preserves the real brain signal in response to visual stimulation used here. Changes in glutamate fluorescence of each pixel at each time point were expressed as percent change relative to pre-stimulus baseline window -1000 to -100 ms ($\Delta F/F_0$*100%, where F_0 is the average fluorescence signal during the baseline period, and F is fluorescence at each time point, $\Delta F = F-F_0$).

Application of GSR allowed to remove 8-12 Hz heart-rate related hemodynamic signals which result from the overlapping excitation and emission spectra of green fluorescent proteins and absorption spectrum of hemoglobin[35] (Figure 1D,E). However, GSR left intact a slow, BOLD-

like wave that was locked to the stimulus onset. Slow waves starting around 1 s post-stimulus and lasting for 4-5 seconds have been reported before and are a result of neurovascular coupling[1,35].

To correct for the slow neurovascular response superimposed on ERPs (single-pulse sensory stimulation) and ssVEPs (sine-wave stimulation), we performed *robust detrending*: Iteratively fitting the n-th order polynomial to the data and subtracting it[78,79]. Given that detrending is highly sensitive to sharp amplitude changes in the timeseries such as ERPs (here, generated in response to flicker onset), fitting of which can introduce spurious fluctuations in the detrended signal or even partially removal of a neural signal [78,79], we performed polynomial fitting excluding the first 100 samples (667 ms) after the stimulation onset and offset (for similar approach see van Driel et al.[79]). To perform robust detrending we used *nt_detrend* function from NoiseTools MATLAB toolbox (http://audition.ens.fr/adc/NoiseTools/)[78]. Robust detrending is an iterative procedure, such that a time window in each pixel timeseries is fitted with a high-order polynomial, and residuals between the fit and the raw signal are computed. The fit is then subtracted from the raw signal and time points at which residuals surpass a predefined threshold (3 standard deviations from the mean) are downweighed (weights set to 0) and are not fitted in the next iteration. The maximum number of iterations was set to 3 (default value).

Fitting only the non-ERP parts of the signal was implemented by initially setting the weight vector to 0 during the 0-700 ms windows relative to the stimulus onset and offset. This window was chosen based on: (1) the duration of an ERP in mouse V1 reported using voltage sensitive dye imaging[76], which is not affected by hemodynamics[1] and (2) the onset of to-be-fitted slow wave (negative $\Delta F/F_0$ values started around 500 ms after flicker onset). The higher the order of the polynomial, the smaller the fluctuations that are fitted and subsequently subtracted. Thus, there is a tradeoff between artifact and real signal removal. We empirically tested polynomials with 10, 20, 30 and 50 order, and selected 20 order polynomial, because ERP peak amplitudes were not altered after polynomial removal and computation time was acceptable for these large datasets. The polynomial fitting was done in sliding windows of 100 frames (667 ms), with 50% window overlap.

ssVEP power and phase calculation. ssVEPs are assumed to be stationary narrow-band signals and ssVEP power spectra are typically calculated from trial-average waveforms. However, fluctuations in instantaneous SSVEP frequency indicate cycle-to-cycle variations in response waveforms which would be lost after averaging[9]. For this reason, FFT was performed on single-

trial data and absolute value of FFT coefficients were squared and averaged across trials to obtain ssVEP power spectra. When calculating power spectra, the first 1000 ms relative to flicker onset were excluded, as it contains ERPs and steady-state response takes time to develop[9]. Thus 1000-10000 ms time window (relative to the stimulus onset) was used and zeropadded to obtain 0.1 Hz resolution for power spectra. To facilitate comparison of ssVEPs generated in response to different flicker frequencies, power spectra were converted to SNR units[14]: Ratio between the power at the frequency of interest was divided by the average power at the neighboring frequencies (±1 Hz), excluding 0.5 Hz around the frequency of interest:

$$SNR(f) = \frac{F(f)}{\frac{1}{2N}\sum_{k=\pm 6,\pm 7,\dots,\pm N} F(f + \Delta f \cdot k)}$$

where Δf = 0.1 Hz, N = ± 1 Hz (10 bins).

We also used FFT analysis on trial-average data to obtain phase maps by computing the angle between real and imaginary part of complex Fourier coefficients at each flicker frequency of interest for each pixel. In this case, we used trial-average data because of higher signal-to-noise ratio for phase estimation.

ssVEP spatiotemporal pattern analysis. Spatially variable patterns in average power and phase maps indicated that the spatial distribution of ssVEPs depended on flicker frequency. However, power and phase maps derived from FFT over the entire trial window discard temporal amplitude fluctuations and provide only a static view. Thus, in the follow up spatiotemporal pattern analysis we combined temporal and spatial properties of ssVEPs by narrow-band pass filtering the data around the flicker frequency and using two-stage eigenvalue decomposition on covariance matrices (detailed illustration of analysis steps is depicted in Supplementary Figure 9). The end goal of this procedure was to compute a set of pixel weights (empirical spatial filters) that multiplied by the pixel time series maximally separate the signal data (frequency-specific response to flicker) from the reference data (brain response to spectrally adjacent non-flicker frequencies). Given the high number of dimensions (~8000 pixels containing brain data), matrix operations are computationally heavy and can result in numerically unstable solutions[80]. Therefore, we first reduced data dimensionality using PCA and then performed generalized eigenvalue decomposition (GED) to identify spatiotemporal patterns characteristic to specific temporal frequency stimulation.

In the first step, for each flicker frequency single-trial covariance matrices across brain pixels (M number of brain pixels) were calculated and averaged. The time window for covariance matrix calculation was restricted to 1000-10000 ms (relative to flicker onset). PCA was performed on this trial-average covariance matrix and eigenvalues were converted to percent total variance explained and only PCs that explain more than 0.01% of total variance were retained (N number of PCs). PC component time series were reconstructed as follows:

$$\boldsymbol{Y} = V_{1:N}^{T} X$$

where V are PCA eigenvectors and X is the data matrix pixels x time x trials, N is a number of retained PCs.

In the second step, we performed generalized eigenvalue decomposition (GED) to find spatiotemporal patterns in pixel covariance matrices that are characteristic to specific temporal frequency response. This was implemented by finding a linear weighted sum over all brain pixels that would result in the highest multivariate signal-to-noise ratio. The "signal" (**S**) here is the response to flicker frequency, and "noise" or "reference" (**R**) is the signal at spectrally adjacent non-flicker frequencies. In practice, this was done by eigenvalue decomposition of the matrix product R^{-1} S and solving the equation:

$$SW = RW\Lambda$$

where **S** and **R** are covariance matrices, **W** is the matrix of eigenvectors and **Λ** is a diagonal matrix of eigenvalues.

The **S** and **R** covariance matrices were constructed as follows. First, PC time series **Y** were narrow band-pass filtered using Gaussian filters: (1) centered at the flicker frequency *f* with FWHM = 0.5 Hz; (2) filter centered at *f* - 2 Hz with FWHM = 2 Hz; and (3) filter centered at *f* + 2 Hz with FWHM = 2 Hz. Data filtered at the flicker frequency is further referred to as "signal" (S), and data filtered at the neighboring frequencies is referred to as "reference" (R). Single-trial temporally-filtered data from 1000-10000 time window (relative to flicker onset) were concatenated and were used to compute *N* by *N* covariance matrices: one **S** matrix and two **R** matrices that were averaged. When computing covariance matrices, the first 1000 ms after flicker onset were excluded, because the quality of GED spatial filters (columns of the matrix **W**) is poorer when sharp transient responses to flicker onset are included[31]. Covariance matrix **R** was shrinkage regularized by adding 1% of its average eigenvalues (0.01*mean(eig(R))) to the diagonal of the **R** matrix prior to GED[80]. Shrinkage regularization reduces the influence of noise on the GED. GED

performed on covariance matrices **S** and **R** returned a matrix of eigenvectors (**W**) and a diagonal matrix of eigenvalues (**Λ**). Eigenvector **w** (spatial filter) associated with the highest eigenvalue λ was multiplied by "signal" covariance matrix **S** to extract the spatial response pattern characteristic to a specific flicker frequency, and right multiplied by PC vectors (1 to N) to get back from principal component space to pixel space: $w^T S\, V_{1:N}^T$.

Wave propagation analysis. To quantify and visualize stimulus-evoked travelling and standing waves we used phase latency method (https://github.com/mullerlab/wave-matlab)[32]. To increase the signal-to-noise ratio, we first re-epoched ssVEP data relative to every 5th peak in the stimulus sine-wave (excluding the first 1000 ms containing stimulus-onset ERP) and averaged these short epochs. Thereafter, we narrow band-pass filtered the data using Gaussian filters centered at the flicker frequency with FWHM = 1 Hz. Pulse ERP data was band-passed filtered (5-25 Hz) using forward-reverse fifth-order Butterworth filter. After filtering the ssVEP and ERP data, we extracted instantaneous phase at each pixel using a Hilbert transform. Thereafter, we computed the phase offset (in milliseconds) relative to the timeframe prior to the first ERP peak[32], this ensures that phase latency maps represent phase relationships over space at the timeframe of ssVEP or ERP peak. The minimum of the phase latency map was taken as the wave source. For ssVEP data, phase latency maps were computed only for low-frequency conditions (<13 Hz), as high frequency flicker stimulation rendered phase-based analyses impossible. Phase latency maps were smoothed only for representation purposes (robust spline smoothing[81]), unsmoothed phase latency was used for wave velocity calculations.

To compute the wave velocity, we performed a linear fit to the phase latency and distance (within 1000 μm radius from the wave source) relationship along 16 directions (0, 30, 45, 60, 90, 120, 135, 150, 180, 210, 225, 240, 270, 300, 315, 330 deg). The inverse of the linear fit slope was taken as a wave propagation speed. For each animal, we only considered directions along which phase latency was monotonically increasing from the wave source. For some animals, wave speed for directions around anterior-posterior axis (90, 120, and 270 deg) could not be computed due to close proximity of the wave source to the V1 border and thus these directions are not represented in the group average plot in Figure 4D.

Statistical analyses

Evaluating statistical significance of ssVEPs. To evaluate statistical significance of ssVEP responses, for each flicker condition the power spectra were calculated using trials on which neither the flicker frequency nor harmonically related frequencies were presented. This allowed us to evaluate what level of SNR can be expected without visual stimulation at that frequency ("noise" SNR distribution). On average, "noise" SNR distribution was built from 261 trials (SD = 25.37). The 95th percentile of "noise" SNR distribution is plotted in Figure 2D and referred to as "H0 hypothesis".

Cortical map statistics. To evaluate and compare the spatial extent of responses across different flicker frequencies, power maps at the flicker frequency ("signal") were compared against adjacent conditions when that flicker frequency was not present ("noise"). For example, 7 Hz ssVEPs signal (10 trials) was compared against 7 Hz activity elicited when stimulus flickered at 6 Hz and 8 Hz (20 trials in total). Three different techniques were used to generate null-hypothesis (H0) distribution: (1) drawing "signal" and "noise" condition trials by resampling with replacement (bootstrap) from all trials pooled together[82]; (2) resampling without replacement (permutation testing) by permuting all the trials and randomly assigning a condition label[83], and (3) bootstrap-t technique, in which the two conditions are mean-centered and bootstrapped samples are drawn from the two conditions separately. Given the statistical robustness of bootstrap-t approach for small sample sizes, independence of each draw and almost identical results of all three resampling approaches, results on bootstrap-t are reported here. The procedure is illustrated in Supplementary Figure 5 and was performed in the following steps.

First, cortical maps of "signal" trials and "noise" trials were z-scored, and two-sample t-test performed at each pixel to obtain the *observed* t-values. Thereafter, signal and noise trials were mean-centered. Second, two groups of trials were separately sampled with replacement and a t-test performed for each bootstrap (1000 iterations), thus building a distribution of *bootstrapped* t-values. Third, the observed t-values were z-scored using the mean and SD of bootstrapped t-values. Fourth, SNR differences between conditions were considered statistically significant if the z-scored t-value at each pixel in the cortical map was larger than 3.0902 ($p < 0.001$). Finally, cluster-based correction was applied to correct for multiple comparisons over pixels, such that only contiguous pixel islands (clusters) that were larger in size than 99% of H0 cluster size distribution

were considered significant. The H0 distribution of cluster sizes was obtained by thresholding cortical maps from each of the 1000 iterations at p = 0.01, and storing the maximum cluster extent (sum of t-values within a cluster). Clusters of contiguous pixels in the observed t-value cortical maps were considered significant if the cluster size was bigger than expected under the null hypothesis. To obtain more stable estimates of cluster significance, we ran a "meta-permutation test" by repeating pixel-level and cluster-level permutation procedure 20 times. Thus, the average of 20 real z-scored t-values and the average of 20 cluster thresholds were used.

ssVEP spatiotemporal patterns. To identify similarities across cortical maps elicited by different flicker frequencies, we computed pairwise correlations between frequency-specific spatiotemporal patterns identified using a two-stage GED (see subsection *ssVEP spatiotemporal pattern analysis*). These correlation matrices, a prominent feature of which is a block diagonal form, were submitted to hierarchical clustering which allowed to group ssVEP cortical maps and identify characteristic spatiotemporal patterns. To facilitate clustering, the correlation matrices were squared. To build a hierarchical tree (dendrogram), we performed agglomerative clustering using Ward's minimum variance criterion which minimizes the total within-cluster variance (Matlab function *linkage*). The hierarchical tree was then pruned by setting the number of lower branches (leaf nodes) to maximum 4, which was determined empirically and allowed to distinguish 4-6 clusters of spatiotemporal patterns per animal.

Modelling standing waves

A linear wave equation. As noted in the main text, we explored whether empirically observed standing wave patterns could be approximated by a classical d'Alembert's wave equation with a damping term:

$$\ddot{w}(x,t) = c^2\nabla^2 w(x,t) - 2d\dot{w}(x,t) + u(x,t) \tag{1}$$

where $w(x,t)$ are the observed spatiotemporal wave responses at time t and cortical position $\boldsymbol{x} = \{x1, x2\}$, and ∇^2 is the spatial Laplacian operator which sums the second spatial derivatives in x_1 and x_2. The discrete Laplacian in 1D corresponds to convolution with the kernel $\{1, -2, 1\}$, where a "restoring force" is proportional to the wave's displacement at each location x relative to its neighbors. We included a viscous damping force $-2d\dot{w}(x,t)$ which attenuates the wave response over time. Parameter c is related to the wave propagation velocity and d to the wave damping. We

chose $2d$ rather than d to simplify the expression for dispersion relation (see the next section "*Dispersion relation*"). We modelled the flickering stimulus as a spatiotemporally separable product of a spatial component $u(x)$ with temporal modulation $u(t)$, i.e. $u(x,t) = u(x)\,u(t)$. Parameters c and d were determined using a fitting procedure based on the empirical data (see section "*Estimating dispersion relation*").

Dispersion relation. A linear wave equation such as in equation (1) makes specific predictions about the relationship between the temporal frequency of the flickering stimulus and evoked spatial modes (a dispersion relation). The spatial component of separable solutions to a linear wave equation are eigenmodes of the Laplace operator ∇^2. Each eigenmode has a characteristic spatial and temporal frequency, and thus indicates which standing wave patterns can be expected to form at various temporal stimulation frequencies.

To derive a dispersion relation and compute the eigenmodes, we performed change of basis to diagonalize equation (1). We used the two-sided Laplace transform for the temporal basis, expressed as: $\xi(s) = \int w(t)\, e^{-st}\, dt$, which is related to the unitary Fourier transform in angular frequency ω by the substitution $s \leftarrow i\omega$. The spatial basis consists of eigenfunctions $\phi_k(x)$ (indexed by k) of the Laplacian operator ∇^2. These eigenfunctions satisfy the eigenvalue equation $\eta_k \phi_k(x) = \nabla^2 \phi_k(x)$, with eigenvalue η_k. On an infinite (or rectangular periodic) domain, these are plane waves. Here, however, the domain was nearly circular patch of cortex and Laplacian eigenmodes were solved numerically (see section "*Defining region of cortex for modelling spatial eigenmodes*").

Switching to the Laplace domain in time and the Laplacian eigenfunctions in space, equation (1) becomes:

$$s^2 \xi(s,k) = [c^2 \eta_k - 2d]\,\xi(s,k) + \upsilon(s)\upsilon_k \tag{2}$$

where $\upsilon(s)$ and υ_k are the projections of the input's temporal and spatial components onto Fourier-Laplace basis and Laplacian eigenspace, respectively. Note that the Laplace transform of the time derivative is simply s. Collecting terms in (2) and solving for $\xi(s,k)$ gives the following transfer function $g(s,k)$ from stimulus (υ) to the spatiotemporal wave response (ξ):

$$\xi(s,k) = g(s,k)\,\upsilon(s)\upsilon_k \tag{3}$$

$$g(s,k) = 1/[s^2 + 2ds - c^2 \eta_k] \tag{4}$$

The system's modes are given by the poles of this transfer function, i.e. when the denominator of *g(s,k)* is zero. Solving for *s*, we get:

$$s = -d \pm \sqrt{d^2 + c^2 \eta_k} \tag{5}$$

Oscillating solutions appear when $s = -d \pm i\omega$ is complex, which occurs when $d^2 + c^2\eta_k < 0$. The real part of these solutions, $-d$, determines how quickly modes decay in time. The imaginary component determines the oscillation frequency ω (radians/second), and solutions always appear in conjugate pairs with a positive and negative ω:

$$\omega = \pm\sqrt{-d^2 - c^2\eta_k} \tag{6}$$

By squaring both sides of the equation (6), we obtain relationship between Laplacian eigenvalue η to the square of the temporal frequency ω:

$$\omega^2 = -c^2\eta_k - d^2 \tag{7}$$

The Laplacian eigenvalues η_k have a more intuitive interpretation on an infinite or square periodic domain. In this case, the eigenfunctions $\phi_k(x)$ of the Laplacian are the spatial Fourier modes (i.e. plane waves). The Laplacian eigenvalues are $\eta_{\boldsymbol{\nu}} = -\|\boldsymbol{\nu}\|^2$, where $\boldsymbol{\nu} = \{\nu 1, \nu 2\}$ are the angular spatial frequencies for each spatial dimension, and $\|\boldsymbol{\nu}\|$ is the overall angular spatial frequency of the given wave component. Even though here spatial eigenfunctions are not plane waves, it is convenient to express spatial angular frequency as $|\nu| = \sqrt{-\eta_\nu}$ (in units of radians per mm), and wavelength as $\lambda = 2\pi/|\nu| = 2\pi\sqrt{-\eta_\nu}$ (in units of mm per cycle). By expressing $\eta_{\boldsymbol{\nu}}$ as $\eta_{\boldsymbol{\nu}} = -(2\pi/\lambda)^2$, relationship between the wavelength λ of the spatial pattern and flicker frequency ω can be obtained (Figure 5E). We report λ in units of millimeters per cycle and ω in units of Hz.

Defining region of cortex for modelling spatial eigenmodes. Based on visual inspection, spatiotemporal patterns extracted using two-stage eigenvalue decomposition elicited by 3 Hz and 30 Hz flicker stimuli contained spatially well-defined near-zero amplitude contours. Therefore, we used the union of regions excited by these two flicker conditions to define the excited region of posterior cortex. The region was defined separately for each animal. The extracted regions were roughly circular, spanning 3.9–4.3 mm along the anterior-posterior axis, and 3.7–4.4 mm along

the mediolateral axis (Supplementary Figure 12). Alignment with the Allen CCF indicated that this region includes the extended visual cortex (V1 and several higher-level visual areas).

Calculating Laplacian eigenmodes. Calculation of Laplacian eigenmodes requires to define how travelling waves interact with areal boundaries. Given the phase reversal in phase maps and near-zero ssVEP amplitude near the boundary, we assumed Dirichlet type boundary conditions of the modelled region.

We constructed a matrix representing a discrete Laplace operator on the region of posterior cortex excited by the flickering stimuli (a region of 55–65 pixels width and height, containing 3306–4160 pixels each). For this, we first constructed an adjacency matrix (**A**), which describes neighborhood relation between pixels in a modelled region and is a symmetric matrix. For example, if pixel *i* and *j* are neighbors, the entry in row *i* and column *j* (and row *j* and column *i*) of the adjacency matrix will be 1. The matrix form of discrete Laplace operator then can be defined as **L = A-D**, where **D** is degree matrix, which is a diagonal matrix and indicates the total number of neighbors a pixel has and is calculated as the sum of the ith row of the adjacency matrix. We divided the resulting matrix **L** by the squared grid spacing (223 mm^{-2}), giving this matrix physical units of a second spatial derivative. We used sparse matrix formats and Scipy's sparse linear algebra routines to calculate the eigenvectors υ_k and eigenvalues of η_k of this discrete Laplacian matrix (scipy.sparse.linalg.eigsh). Exemplar eigenmodes from one animal are shown in Figure 5A and are compared to spatiotemporal patterns extracted using two-stage GED procedure.

Eigenvalue spectra. We quantified the extent to which each Laplacian eigenmode was triggered by a particular flicker frequency ω by computing the similarity between the two cortical maps. For this, at each pixel $\boldsymbol{x}$ we performed FFT on single-trial data and extracted complex Fourier coefficients $\boldsymbol{z}_{\omega,\boldsymbol{x}}$ at the flicker frequency ω. We normalized each $\boldsymbol{z}_{\omega,\boldsymbol{x}}$ to unit length ($\widehat{z_{\omega,\mathrm{x}}} = z_{\omega,\mathrm{x}}/\|z_{\omega,\mathrm{x}}\|$) to account for the power-law scaling (decrease in response amplitude with increased frequency). We then calculated the variance in $\widehat{z_{\omega,\mathrm{x}}}$ explained by eigenmode $\boldsymbol{\upsilon}_{k,\boldsymbol{x}}$ by computing squared dot product $p_{\omega,\mathrm{x}} = \left|\langle \widehat{z_{\omega,\mathrm{x}}}, \nu_{k,\omega}\rangle\right|^2$. This way we obtained eigenvalue spectra: one for each eigenmode (Figure 5C). The eigenvalue spectra were smoothed with a Gaussian kernel (σ = 5 Hz). In Figure 5C, we report normalized eigenvalue spectra for each eigenmode in units of power density per Hz.

The approximately circular 2D domain contains eigenmodes with similar eigenvalues. For example, the “four-lobe” pattern appears as two eigenmodes, with one rotated by 45°relative to another. Focal stimulation will excite a linear combination of these degenerate eigenmode pairs. For these paired modes, we averaged the eigenvalue spectra and associated this average eigenvalue spectrum with the average of the corresponding eigenvalues.

Estimating dispersion relation. To identify parameters of the wave equation, we took a heuristic approach rather than fitting ssVEP responses from each pixel and each flicker frequency to the damped wave equation (1). For this, we used eigenvalue spectra to identify a range of temporal stimulus frequencies (ω) associated with an eigenmode k and its corresponding Laplacian eigenvalue η_k. This was done by fitting a locally-quadratic model to the most prominent peak in eigenvalue spectra (Figure 5C). To fit this model, we used all points between the "edges" of each peak, defined as the inflection points in the log-power spectrum adjacent to each local maximum. We used the peak of this quadratic fit as a proxy for a fundamental driving frequency ω associated with an eigenmode k. In cases when eigenvalue spectra contained multiple peaks, we selected a single peak satisfying the following constraints. First, we excluded the peaks that were 25% smaller than the maximal peak. Second, we assumed that Laplacian eigenvalues η_k and spatial frequency of evoked standing waves should monotonically increase with increasing flicker frequency ω, thus we discarded peaks that did not satisfy this constraint. We then combined data across animals and fitted dispersion relation derived from equation (1), thus mapping Laplacian eigenvalue η_k to the squared temporal frequency ω_k^2 and estimating parameters c and d in equation (7).

ACKNOWLEDGEMENTS

Rasa Gulbinaite has received funding from the European Union’s Horizon 2020 research and innovation programme under the Marie Skłodowska-Curie grant agreement No. 843379. Michael E. Rule is supported by a Leverhulme and Isaac Newton Trust fellowship ECF-2020-352.

REFERENCES

1. Carandini, M., Shimaoka, D., Rossi, L.F., Sato, T.K., Benucci, A., and Knöpfel, T. (2015). Imaging the awake visual cortex with a genetically encoded voltage indicator. J Neurosci *35*, 53–63. 10.1523/JNEUROSCI.0594-14.2015.
2. Crevier, D.W., and Meister, M. (1998). Synchronous period-doubling in flicker vision of salamander and man. J Neurophysiol *79*, 1869–1878. 10.1152/jn.1998.79.4.1869.
3. Nakayama, K., and Mackeben, M. (1982). Steady state visual evoked potentials in the alert primate. Vision Res *22*, 1261–1271. 10.1016/0042-6989(82)90138-9.
4. Rager, G., and Singer, W. (1998). The response of cat visual cortex to flicker stimuli of variable frequency. Eur J Neurosci *10*, 1856–1877. 10.1046/j.1460-9568.1998.00197.x.
5. Regan, D. (1977). Steady-state evoked potentials. J Opt Soc Am *67*, 1475–1489. 10.1364/josa.67.001475.
6. van Swinderen, B. (2012). Competing visual flicker reveals attention-like rivalry in the fly brain. Front Integr Neurosci *6*, 96. 10.3389/fnint.2012.00096.
7. Regan, D. (1968). A high frequency mechanism which underlies visual evoked potentials. Electroencephalogr Clin Neurophysiol *25*, 231–237. 10.1016/0013-4694(68)90020-5.
8. Tsoneva, T., Garcia-Molina, G., and Desain, P. (2015). Neural dynamics during repetitive visual stimulation. J Neural Eng *12*, 066017. 10.1088/1741-2560/12/6/066017.
9. Gulbinaite, R., Roozendaal, D.H.M., and VanRullen, R. (2019). Attention differentially modulates the amplitude of resonance frequencies in the visual cortex. Neuroimage *203*, 116146. 10.1016/j.neuroimage.2019.116146.
10. Notbohm, A., Kurths, J., and Herrmann, C.S. (2016). Modification of Brain Oscillations via Rhythmic Light Stimulation Provides Evidence for Entrainment but Not for Superposition of Event-Related Responses. Front Hum Neurosci *10*, 10. 10.3389/fnhum.2016.00010.
11. Lakatos, P., Gross, J., and Thut, G. (2019). A New Unifying Account of the Roles of Neuronal Entrainment. Curr Biol *29*, R890–R905. 10.1016/j.cub.2019.07.075.
12. Reinhold, K., Lien, A.D., and Scanziani, M. (2015). Distinct recurrent versus afferent dynamics in cortical visual processing. Nat Neurosci *18*, 1789–1797. 10.1038/nn.4153.
13. Schneider, M., Tzanou, A., Uran, C., and Vinck, M. (2023). Cell-type-specific propagation of visual flicker. 2023.01.04.522738. 10.1101/2023.01.04.522738.
14. Norcia, A., Appelbaum, L., Ales, J., Cottereau, B., and Rossion, B. (2015). The steady-state visual evoked potential in vision research: A review. Journal of vision *15*. 10.1167/15.6.4.
15. Adaikkan, C., Middleton, S.J., Marco, A., Pao, P.-C., Mathys, H., Kim, D.N.-W., Gao, F., Young, J.Z., Suk, H.-J., Boyden, E.S., et al. (2019). Gamma Entrainment Binds Higher-Order Brain Regions and Offers Neuroprotection. Neuron *102*, 929-943.e8. 10.1016/j.neuron.2019.04.011.
16. Soula, M., Martín-Ávila, A., Zhang, Y., Dhingra, A., Nitzan, N., Sadowski, M.J., Gan, W.-B., and Buzsáki, G. (2023). Forty-hertz light stimulation does not entrain native gamma oscillations in Alzheimer's disease model mice. Nat Neurosci *26*, 570–578. 10.1038/s41593-023-01270-2.
17. Sun, P., Ueno, K., Waggoner, R.A., Gardner, J.L., Tanaka, K., and Cheng, K. (2007). A temporal frequency–dependent functional architecture in human V1 revealed by high-resolution fMRI. Nat Neurosci *10*, 1404–1406. 10.1038/nn1983.
18. Chai, Y., Handwerker, D.A., Marrett, S., Gonzalez-Castillo, J., Merriam, E.P., Hall, A., Molfese, P.J., and Bandettini, P.A. (2019). Visual temporal frequency preference shows a

distinct cortical architecture using fMRI. Neuroimage *197*, 13–23. 10.1016/j.neuroimage.2019.04.048.
19. Dumoulin, S.O., Harvey, B.M., Fracasso, A., Zuiderbaan, W., Luijten, P.R., Wandell, B.A., and Petridou, N. (2017). In vivo evidence of functional and anatomical stripe-based subdivisions in human V2 and V3. Sci Rep *7*, 733. 10.1038/s41598-017-00634-6.
20. Issa, N.P., Rosenberg, A., and Husson, T.R. (2008). Models and measurements of functional maps in V1. J Neurophysiol *99*, 2745–2754. 10.1152/jn.90211.2008.
21. Sato, T.K., Nauhaus, I., and Carandini, M. (2012). Traveling waves in visual cortex. Neuron *75*, 218–229. 10.1016/j.neuron.2012.06.029.
22. Muller, L., Chavane, F., Reynolds, J., and Sejnowski, T.J. (2018). Cortical travelling waves: mechanisms and computational principles. Nat Rev Neurosci *19*, 255–268. 10.1038/nrn.2018.20.
23. Billock, V.A., and Tsou, B.H. (2012). Elementary visual hallucinations and their relationships to neural pattern-forming mechanisms. Psychol Bull *138*, 744–774. 10.1037/a0027580.
24. Rule, M., Stoffregen, M., and Ermentrout, B. (2011). A model for the origin and properties of flicker-induced geometric phosphenes. PLoS Comput Biol *7*, e1002158. 10.1371/journal.pcbi.1002158.
25. Burkitt, G.R., Silberstein, R.B., Cadusch, P.J., and Wood, A.W. (2000). Steady-state visual evoked potentials and travelling waves. Clin Neurophysiol *111*, 246–258. 10.1016/s1388-2457(99)00194-7.
26. Srinivasan, R., Bibi, F.A., and Nunez, P.L. (2006). Steady-state visual evoked potentials: distributed local sources and wave-like dynamics are sensitive to flicker frequency. Brain Topogr *18*, 167–187. 10.1007/s10548-006-0267-4.
27. Zhigalov, A., and Jensen, O. (2023). Perceptual echoes as travelling waves may arise from two discrete neuronal sources. Neuroimage *272*, 120047. 10.1016/j.neuroimage.2023.120047.
28. Lozano-Soldevilla, D., and VanRullen, R. (2019). The Hidden Spatial Dimension of Alpha: 10-Hz Perceptual Echoes Propagate as Periodic Traveling Waves in the Human Brain. Cell Rep *26*, 374-380.e4. 10.1016/j.celrep.2018.12.058.
29. Tsoneva, T., Garcia-Molina, G., and Desain, P. (2021). SSVEP phase synchronies and propagation during repetitive visual stimulation at high frequencies. Sci Rep *11*, 4975. 10.1038/s41598-021-83795-9.
30. Marvin, J.S., Borghuis, B.G., Tian, L., Cichon, J., Harnett, M.T., Akerboom, J., Gordus, A., Renninger, S.L., Chen, T.-W., Bargmann, C.I., et al. (2013). An optimized fluorescent probe for visualizing glutamate neurotransmission. Nat Methods *10*, 162–170. 10.1038/nmeth.2333.
31. Cohen, M.X., and Gulbinaite, R. (2017). Rhythmic entrainment source separation: Optimizing analyses of neural responses to rhythmic sensory stimulation. Neuroimage *147*, 43–56. 10.1016/j.neuroimage.2016.11.036.
32. Muller, L., Reynaud, A., Chavane, F., and Destexhe, A. (2014). The stimulus-evoked population response in visual cortex of awake monkey is a propagating wave. Nat Commun *5*, 3675. 10.1038/ncomms4675.
33. Xie, Y., Chan, A.W., McGirr, A., Xue, S., Xiao, D., Zeng, H., and Murphy, T.H. (2016). Resolution of High-Frequency Mesoscale Intracortical Maps Using the Genetically Encoded Glutamate Sensor iGluSnFR. J Neurosci *36*, 1261–1272. 10.1523/JNEUROSCI.2744-15.2016.

34. Nazari, M., Karimi Abadchi, J., Naghizadeh, M., Bermudez-Contreras, E.J., McNaughton, B.L., Tatsuno, M., and Mohajerani, M.H. (2023). Regional variation in cholinergic terminal activity determines the non-uniform occurrence of cortical slow waves during REM sleep in mice. Cell Rep *42*, 112450. 10.1016/j.celrep.2023.112450.
35. Valley, M.T., Moore, M.G., Zhuang, J., Mesa, N., Castelli, D., Sullivan, D., Reimers, M., and Waters, J. (2020). Separation of hemodynamic signals from GCaMP fluorescence measured with wide-field imaging. J Neurophysiol *123*, 356–366. 10.1152/jn.00304.2019.
36. Wang, Q., Ding, S.-L., Li, Y., Royall, J., Feng, D., Lesnar, P., Graddis, N., Naeemi, M., Facer, B., Ho, A., et al. (2020). The Allen Mouse Brain Common Coordinate Framework: A 3D Reference Atlas. Cell *181*, 936-953.e20. 10.1016/j.cell.2020.04.007.
37. Donoghue, T., Haller, M., Peterson, E.J., Varma, P., Sebastian, P., Gao, R., Noto, T., Lara, A.H., Wallis, J.D., Knight, R.T., et al. (2020). Parameterizing neural power spectra into periodic and aperiodic components. Nat Neurosci *23*, 1655–1665. 10.1038/s41593-020-00744-x.
38. Senzai, Y., Fernandez-Ruiz, A., and Buzsáki, G. (2019). Layer-Specific Physiological Features and Interlaminar Interactions in the Primary Visual Cortex of the Mouse. Neuron *101*, 500-513.e5. 10.1016/j.neuron.2018.12.009.
39. Nestvogel, D.B., and McCormick, D.A. (2022). Visual thalamocortical mechanisms of waking state-dependent activity and alpha oscillations. Neuron *110*, 120-138.e4. 10.1016/j.neuron.2021.10.005.
40. Karalis, N., and Sirota, A. (2022). Breathing coordinates cortico-hippocampal dynamics in mice during offline states. Nat Commun *13*, 467. 10.1038/s41467-022-28090-5.
41. Waters, J., Lee, E., Gaudreault, N., Griffin, F., Lecoq, J., Slaughterbeck, C., Sullivan, D., Farrell, C., Perkins, J., Reid, D., et al. (2019). Biological variation in the sizes, shapes and locations of visual cortical areas in the mouse. PLoS One *14*, e0213924. 10.1371/journal.pone.0213924.
42. Polack, P.-O., and Contreras, D. (2012). Long-range parallel processing and local recurrent activity in the visual cortex of the mouse. J Neurosci *32*, 11120–11131. 10.1523/JNEUROSCI.6304-11.2012.
43. Benucci, A., Frazor, R.A., and Carandini, M. (2007). Standing waves and traveling waves distinguish two circuits in visual cortex. Neuron *55*, 103–117. 10.1016/j.neuron.2007.06.017.
44. Fehérvári, T.D., Okazaki, Y., Sawai, H., and Yagi, T. (2015). In Vivo Voltage-Sensitive Dye Study of Lateral Spreading of Cortical Activity in Mouse Primary Visual Cortex Induced by a Current Impulse. PLoS One *10*, e0133853. 10.1371/journal.pone.0133853.
45. Xu, W., Huang, X., Takagaki, K., and Wu, J. (2007). Compression and reflection of visually evoked cortical waves. Neuron *55*, 119–129. 10.1016/j.neuron.2007.06.016.
46. Andermann, M.L., Kerlin, A.M., Roumis, D.K., Glickfeld, L.L., and Reid, R.C. (2011). Functional specialization of mouse higher visual cortical areas. Neuron *72*, 1025–1039. 10.1016/j.neuron.2011.11.013.
47. Lewis, C.M., Ni, J., Wunderle, T., Jendritza, P., Lazar, A., Diester, I., and Fries, P. (2021). Cortical gamma-band resonance preferentially transmits coherent input. Cell Reports *35*. 10.1016/j.celrep.2021.109083.
48. Niell, C.M., and Stryker, M.P. (2008). Highly selective receptive fields in mouse visual cortex. J Neurosci *28*, 7520–7536. 10.1523/JNEUROSCI.0623-08.2008.
49. Han, X., Vermaercke, B., and Bonin, V. (2022). Diversity of spatiotemporal coding reveals specialized visual processing streams in the mouse cortex. Nat Commun *13*, 3249. 10.1038/s41467-022-29656-z.

50. Umino, Y., Pasquale, R., and Solessio, E. (2018). Visual Temporal Contrast Sensitivity in the Behaving Mouse Shares Fundamental Properties with Human Psychophysics. eNeuro *5*, ENEURO.0181-18.2018. 10.1523/ENEURO.0181-18.2018.
51. Dyballa, L., Hoseini, M.S., Dadarlat, M.C., Zucker, S.W., and Stryker, M.P. (2018). Flow stimuli reveal ecologically appropriate responses in mouse visual cortex. Proc Natl Acad Sci U S A *115*, 11304–11309. 10.1073/pnas.1811265115.
52. Figueira, J.S.B., Kutlu, E., Scott, L.S., and Keil, A. (2022). The FreqTag toolbox: A principled approach to analyzing electrophysiological time series in frequency tagging paradigms. Developmental Cognitive Neuroscience *54*, 101066. 10.1016/j.dcn.2022.101066.
53. Shah, M.R., Alexander, K.R., Ripps, H., and Qian, H. (2010). Characteristics of Period Doubling in the Rat Cone Flicker ERG. Exp Eye Res *90*, 196. 10.1016/j.exer.2009.10.006.
54. Muthukumaraswamy, S.D., Singh, K.D., Swettenham, J.B., and Jones, D.K. (2010). Visual gamma oscillations and evoked responses: variability, repeatability and structural MRI correlates. Neuroimage *49*, 3349–3357. 10.1016/j.neuroimage.2009.11.045.
55. Kissinger, S.T., Pak, A., Tang, Y., Masmanidis, S.C., and Chubykin, A.A. (2018). Oscillatory Encoding of Visual Stimulus Familiarity. J Neurosci *38*, 6223–6240. 10.1523/JNEUROSCI.3646-17.2018.
56. Aggarwal, A., Brennan, C., Luo, J., Chung, H., Contreras, D., Kelz, M.B., and Proekt, A. (2022). Visual evoked feedforward-feedback traveling waves organize neural activity across the cortical hierarchy in mice. Nat Commun *13*, 4754. 10.1038/s41467-022-32378-x.
57. Funayama, K., Hagura, N., Ban, H., and Ikegaya, Y. (2016). Functional Organization of Flash-Induced V1 Offline Reactivation. J Neurosci *36*, 11727–11738. 10.1523/JNEUROSCI.1575-16.2016.
58. Veit, J., Hakim, R., Jadi, M.P., Sejnowski, T.J., and Adesnik, H. (2017). Cortical gamma band synchronization through somatostatin interneurons. Nat Neurosci *20*, 951–959. 10.1038/nn.4562.
59. Hayden, D.J., Montgomery, D.P., Cooke, S.F., and Bear, M.F. (2021). Visual Recognition Is Heralded by Shifts in Local Field Potential Oscillations and Inhibitory Networks in Primary Visual Cortex. J. Neurosci. *41*, 6257–6272. 10.1523/JNEUROSCI.0391-21.2021.
60. Chen, G., Zhang, Y., Li, X., Zhao, X., Ye, Q., Lin, Y., Tao, H.W., Rasch, M.J., and Zhang, X. (2017). Distinct Inhibitory Circuits Orchestrate Cortical beta and gamma Band Oscillations. Neuron *96*, 1403-1418.e6. 10.1016/j.neuron.2017.11.033.
61. Afrashteh, N., Inayat, S., Bermudez-Contreras, E., Luczak, A., McNaughton, B.L., and Mohajerani, M.H. (2021). Spatiotemporal structure of sensory-evoked and spontaneous activity revealed by mesoscale imaging in anesthetized and awake mice. Cell Rep *37*, 110081. 10.1016/j.celrep.2021.110081.
62. Waters, J. (2020). Sources of widefield fluorescence from the brain. Elife *9*, e59841. 10.7554/eLife.59841.
63. Jia, X., Siegle, J.H., Durand, S., Heller, G., Ramirez, T.K., Koch, C., and Olsen, S.R. (2022). Multi-regional module-based signal transmission in mouse visual cortex. Neuron *110*, 1585-1598.e9. 10.1016/j.neuron.2022.01.027.
64. Di Volo, M., and Férézou, I. (2021). Nonlinear collision between propagating waves in mouse somatosensory cortex. Sci Rep *11*, 19630. 10.1038/s41598-021-99057-7.
65. Mohajerani, M.H., Chan, A.W., Mohsenvand, M., LeDue, J., Liu, R., McVea, D.A., Boyd, J.D., Wang, Y.T., Reimers, M., and Murphy, T.H. (2013). Spontaneous cortical activity

alternates between motifs defined by regional axonal projections. Nat Neurosci *16*, 1426–1435. 10.1038/nn.3499.
66. Allefeld, C., Pütz, P., Kastner, K., and Wackermann, J. (2011). Flicker-light induced visual phenomena: frequency dependence and specificity of whole percepts and percept features. Conscious Cogn *20*, 1344–1362. 10.1016/j.concog.2010.10.026.
67. Smythies, J.R. (1959). The Stroboscopic Patterns. I. The dark phase. British Journal of Psychology *50*, 106–116. 10.1111/j.2044-8295.1959.tb00688.x.
68. Smythies, J.R. (1959). The stroboscopic patterns. II. The phenomenology of the bright phase and after-images. Br J Psychol *50*, 305–324. 10.1111/j.2044-8295.1959.tb00710.x.
69. Ermentrout, G.B., and Cowan, J.D. (1979). A mathematical theory of visual hallucination patterns. Biol Cybern *34*, 137–150. 10.1007/BF00336965.
70. Bressloff, P.C., Cowan, J.D., Golubitsky, M., Thomas, P.J., and Wiener, M.C. (2001). Geometric visual hallucinations, Euclidean symmetry and the functional architecture of striate cortex. Philos Trans R Soc Lond B Biol Sci *356*, 299–330. 10.1098/rstb.2000.0769.
71. Shevelev, I.A., Kamenkovich, V.M., Bark, E.D., Verkhlutov, V.M., Sharaev, G.A., and Mikhailova, E.S. (2000). Visual illusions and travelling alpha waves produced by flicker at alpha frequency. Int J Psychophysiol *39*, 9–20. 10.1016/s0167-8760(00)00105-7.
72. Pearson, J., Chiou, R., Rogers, S., Wicken, M., Heitmann, S., and Ermentrout, B. (2016). Sensory dynamics of visual hallucinations in the normal population. Elife *5*, e17072. 10.7554/eLife.17072.
73. Madisen, L., Garner, A.R., Shimaoka, D., Chuong, A.S., Klapoetke, N.C., Li, L., van der Bourg, A., Niino, Y., Egolf, L., Monetti, C., et al. (2015). Transgenic mice for intersectional targeting of neural sensors and effectors with high specificity and performance. Neuron *85*, 942–958. 10.1016/j.neuron.2015.02.022.
74. Mayford, M., Bach, M.E., Huang, Y.-Y., Wang, L., Hawkins, R.D., and Kandel, E.R. (1996). Control of Memory Formation Through Regulated Expression of a CaMKII Transgene. Science *274*, 1678–1683. 10.1126/science.274.5293.1678.
75. Gorski, J.A., Talley, T., Qiu, M., Puelles, L., Rubenstein, J.L.R., and Jones, K.R. (2002). Cortical excitatory neurons and glia, but not GABAergic neurons, are produced in the Emx1-expressing lineage. J Neurosci *22*, 6309–6314. 10.1523/JNEUROSCI.22-15-06309.2002.
76. Bermudez-Contreras, E., Schjetnan, A.G.-P., Luczak, A., and Mohajerani, M.H. (2023). Sensory experience selectively reorganizes the late component of evoked responses. Cereb Cortex *33*, 2626–2640. 10.1093/cercor/bhac231.
77. Karimi Abadchi, J., Nazari-Ahangarkolaee, M., Gattas, S., Bermudez-Contreras, E., Luczak, A., McNaughton, B.L., and Mohajerani, M.H. (2020). Spatiotemporal patterns of neocortical activity around hippocampal sharp-wave ripples. eLife *9*, e51972. 10.7554/eLife.51972.
78. de Cheveigné, A., and Arzounian, D. (2018). Robust detrending, rereferencing, outlier detection, and inpainting for multichannel data. Neuroimage *172*, 903–912. 10.1016/j.neuroimage.2018.01.035.
79. van Driel, J., Olivers, C.N.L., and Fahrenfort, J.J. (2021). High-pass filtering artifacts in multivariate classification of neural time series data. J Neurosci Methods *352*, 109080. 10.1016/j.jneumeth.2021.109080.
80. Cohen, M.X. (2022). A tutorial on generalized eigendecomposition for denoising, contrast enhancement, and dimension reduction in multichannel electrophysiology. Neuroimage *247*, 118809. 10.1016/j.neuroimage.2021.118809.

81. Garcia, D. (2010). Robust smoothing of gridded data in one and higher dimensions with missing values. Computational Statistics & Data Analysis *54*, 1167–1178. 10.1016/j.csda.2009.09.020.
82. Wilcox, R.R., and Rousselet, G.A. (2018). A Guide to Robust Statistical Methods in Neuroscience. Curr Protoc Neurosci *82*, 8.42.1-8.42.30. 10.1002/cpns.41.
83. Maris, E., and Oostenveld, R. (2007). Nonparametric statistical testing of EEG- and MEG-data. J Neurosci Methods *164*, 177–190. 10.1016/j.jneumeth.2007.03.024.

Supplementary Materials

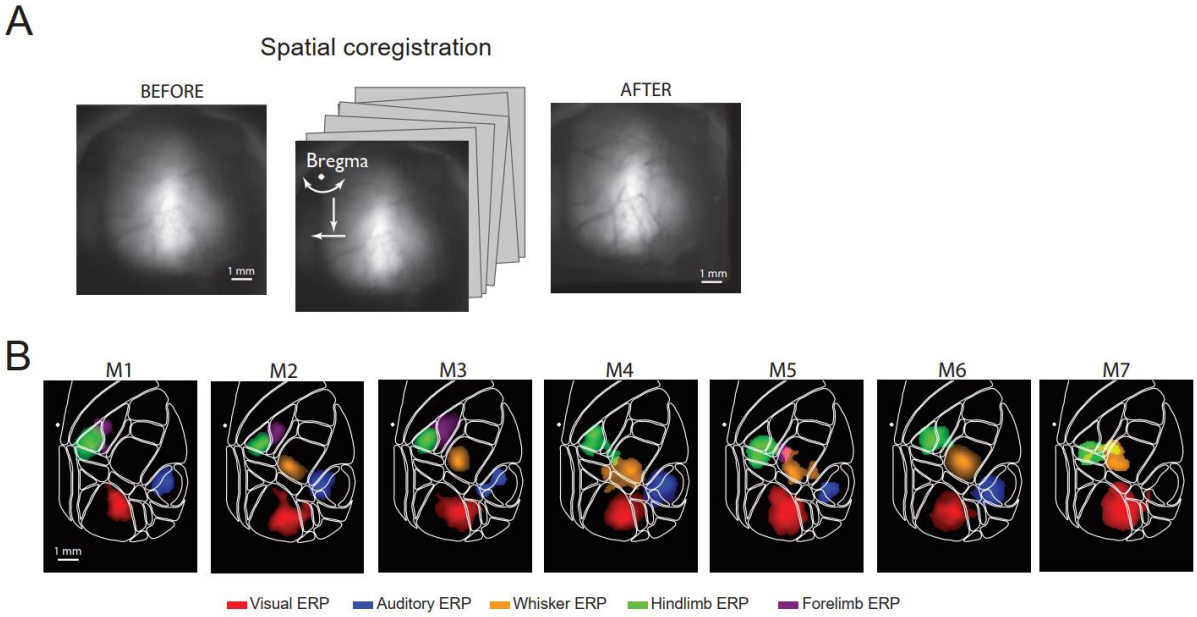

Supplementary Figure 1. Spatial co-registration across recordings and to Allen CCF. (A) Reference images averaged across 5 recording sessions (performed across multiple days) before and after spatial co-registration. Blurry vasculature on the left indicates a slight variability of headfixation of the animal across recordings, which is corrected by rigid image transformation (translation and rotation) on the right. Data from a single animal. (B) Functional maps from all animals representing an overlay of peak evoked activity for different sensory stimuli thresholded at 5 SD relative to the baseline (-1000 – -100 ms relative to the stimulus onset). Sensory stimulation recordings were co-registered to Allen CCF (white outlines) following the same procedure as ssVEP recordings (see Methods section). High correspondence between anatomical areas in Allen CCF and activation peaks over primary sensory areas (VISp, AUDp, SSp-ll, SSp-up, SSp-bfd) shows the quality of alignment to Allen CCF.

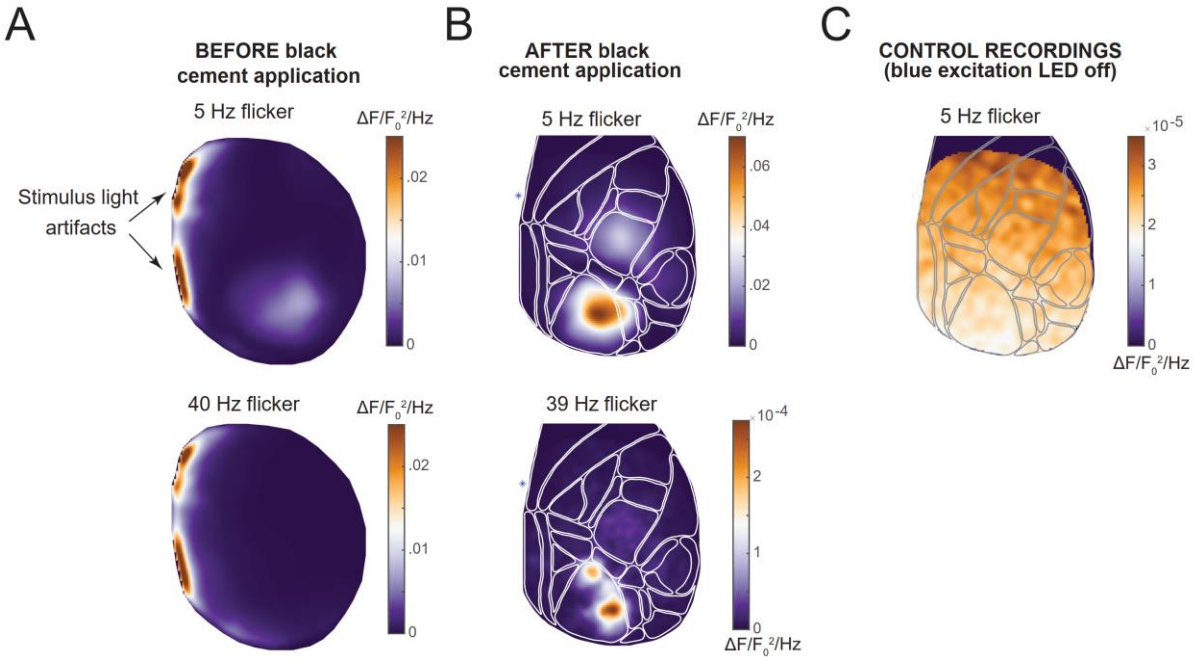

Supplementary Figure 2. Stimulus LED light artifact control. (A) Pilot recordings revealed that despite several measures we have taken to prevent stimulus LED light artifact in the imaging window (3D printed cone fitting the head-ring and black curtain attached to it), the left part of the imaging window was contaminated by the flickering stimulus light (arrows) positioned in the left hemifield. In these recordings, responses to low frequency 5 Hz flicker could be identified (top topography), while visual responses to 40 Hz flicker were not present (bottom topography). We therefore applied an additional layer of black cement over the frontal and lateral parts of the head-plate fixation and the skin. (B) This procedure successfully eliminated light artifacts and revealed responses to high-frequency flicker (bottom topography). (C) At the end of each recording session we also performed control recordings, during which the imaging window was not exposed to excitation blue LED and thus no fluorescence signal should be recorded under such conditions. Under such conditions only stimulus LED artifact should be visible in the imaging area. The power at the flicker frequency was negligible and uniform across the imaging window (compare with topography in B).

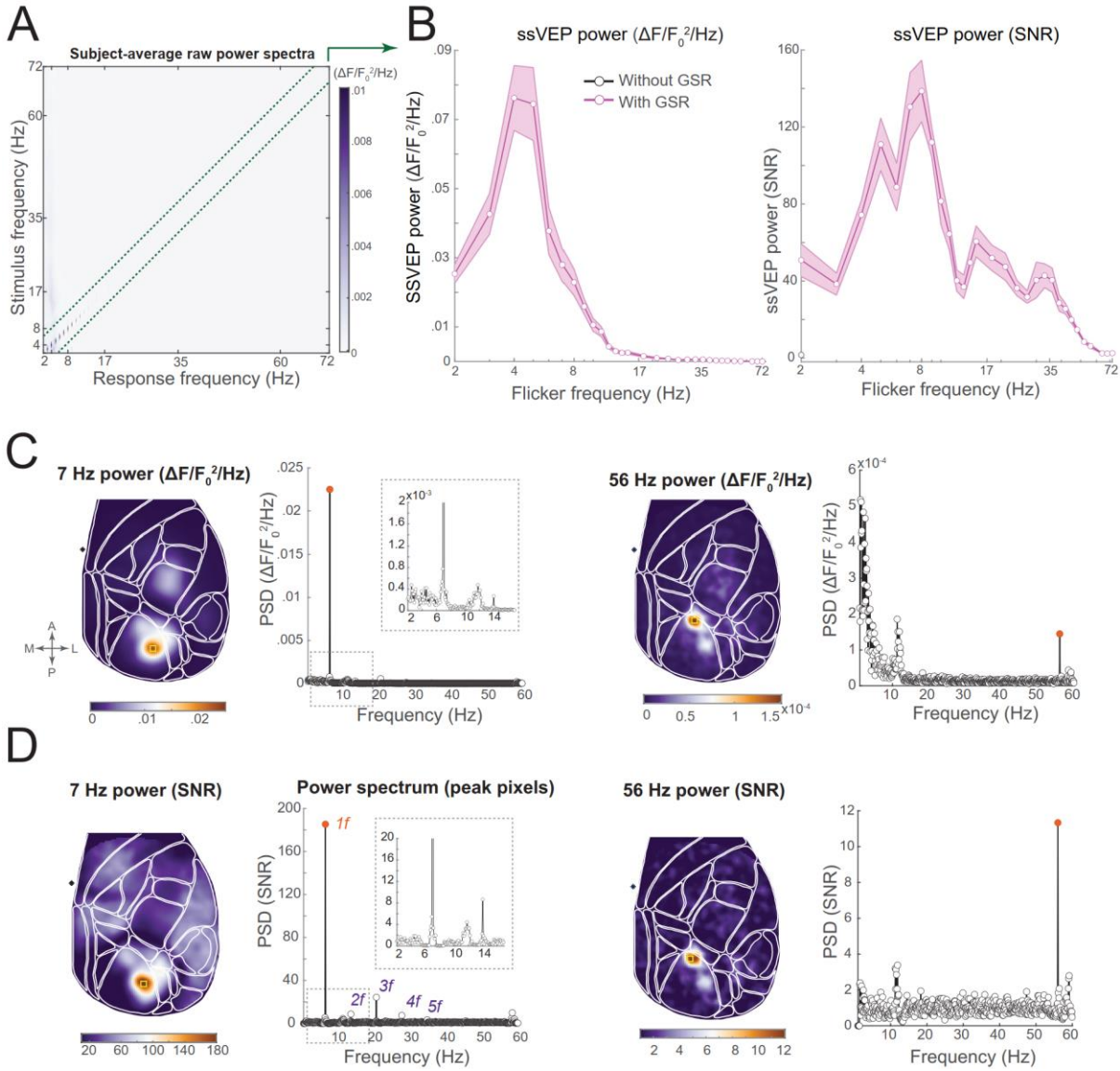

Supplementary Figure 3. Temporal frequency tuning raw power vs. SNR units. (A) Subject-average power spectra (x-axis) expressed in $\Delta F/F_0^2$/Hz units (raw power spectra) plotted as a function of stimulus flicker frequency (y-axis). Note the absence of responses except for the very low flicker frequencies. (B) Left vs. right are temporal frequency tuning curves derived from raw power spectra vs. power spectra that were converted to SNR units (ratio between frequency of interest and the weighted sum of the neighboring frequencies). Note that only a single ~5 Hz peak is visible in temporal frequency tuning curves derived from the raw power spectra. (C) and (D) Exemplar topographies and power spectra from a single animal in response to 7 Hz and 56 Hz flicker stimulation (averaged from 9 pixels around the spatial peak marked as yellow rectangles on the topographies). Top panels: raw power ($\Delta F/F_0^2$/Hz), bottom panels: power expressed in SNR units. Insets: Zoomed in plot of the power spectra around the stimulation frequency.

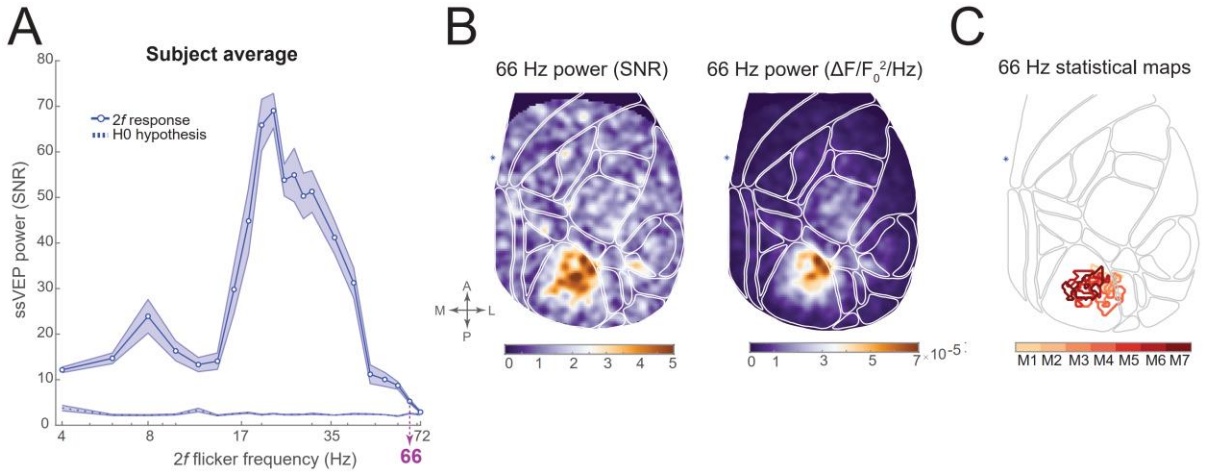

Supplementary Figure 4. 2*f* temporal frequency tuning. (A) Subject-average temporal frequency tuning curve for the 2nd harmonic of the stimulation frequency. ssVEP responses up to 66 Hz (33 Hz flicker stimulation) were statistically significant. Statistical threshold (95th percentile of trials for which flicker frequency of interest was absent) is plotted as a dotted line on the bottom. For comparison, the 1st harmonic responses were significant for flicker frequencies up to 56 Hz. (B) Exemplar ssVEP topographies from a single subject at 66Hz, i.e. the 2nd harmonic response to 33 Hz flicker stimulation (left: SNR, right: raw power $\Delta F/F_0^2$/Hz). (C) Spatial extent of statistically significant 2*f* responses. Data from different animals are plotted in different color contours.

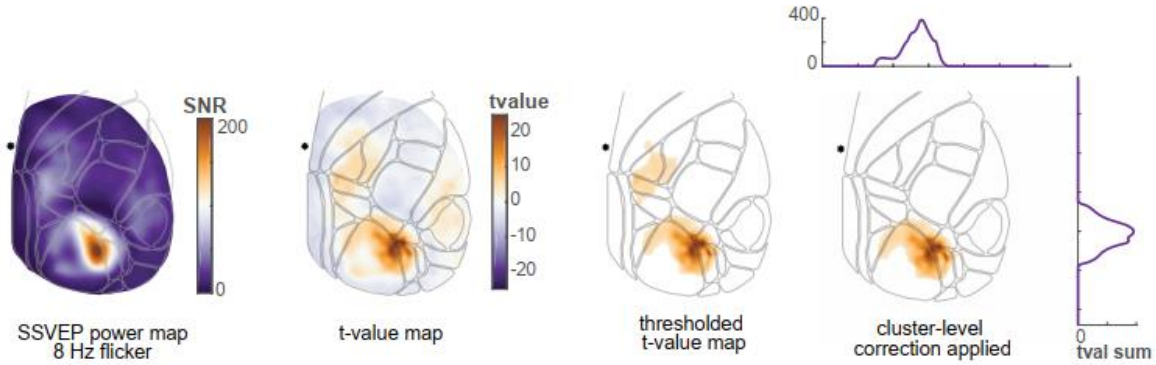

Supplementary Figure 5. Cortical map level statistic using bootstrap-t procedure. Spatial extent of ssVEPs was evaluated using bootstrap-t procedure. For details, see Methods section. Left-most panel, an example of a cortical map in response to 8 Hz flicker (10 trials, one animal). Middle left, color-coded t-value map obtained by performing a paired t-test between 8 Hz ssVEP signal and 8 Hz activity when stimulus flickered at 7 Hz and 9 Hz. Middle right, the same t-value map thresholded at $p = 0.001$. Right-most panel, same t-value map corrected for multiple comparisons across space at $p = 0.01$.

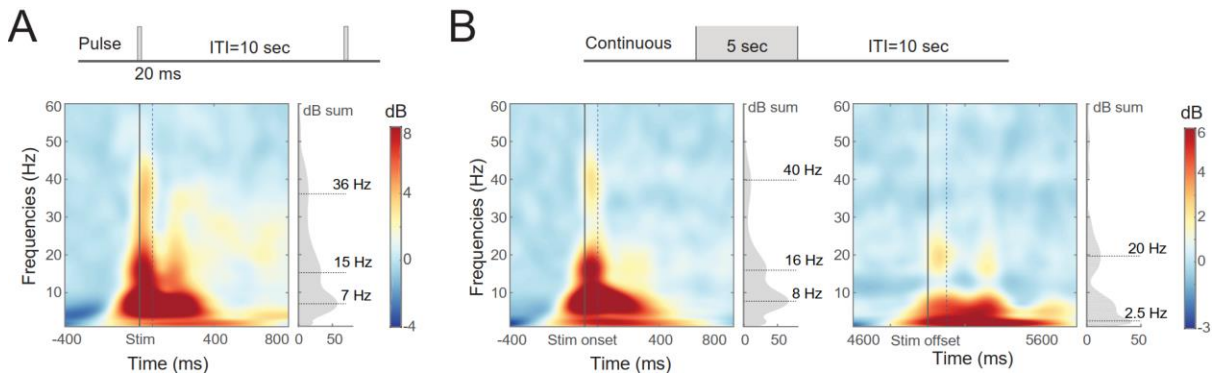

Supplementary Figure 6. Time-frequency representation of responses evoked by pulse (20 ms) and continuous luminance (5 sec) stimuli. (A) Baseline-corrected (-500 – -100 ms) time-frequency representation of responses to pulse and (B) continuous luminance stimuli (subject-average results). Data plotted from V1 ROI (9 pixels around the spatial peak of each event-related potential, ERP). The left and the right graph in (B) represents response to luminance increase (trial onset) or decrease (trial offset) respectively. Spectra in the insets represent power values summed over time window marked with dashed lines (either 0-70 or 0-100 ms in the rightmost graph). Time-frequency decomposition was performed separately for each trial using wavelet transformation, then the trials were averaged and baseline-corrected relative to -500 – -100 ms (where 0 is the stimulus onset). Wavelet transform parameters used in the analysis: 80 linearly spaced frequencies ranging from 1 to 60 Hz in 1 Hz steps, number of wavelet cycles ranged from 3 to 17 and was also linearly spaced. Following pulse and onset of continuous luminance stimuli there was an increase in theta (peak M_{pulse} = 6.97 Hz; $M_{ON\text{-}OFF}$ = 7.72 Hz), beta (M_{pulse} = 15.19 Hz; $M_{ON\text{-}OFF}$ = 15.94 Hz, and gamma power (M_{pulse} = 36.1 Hz; $M_{ON\text{-}OFF}$ = 39.84 Hz).

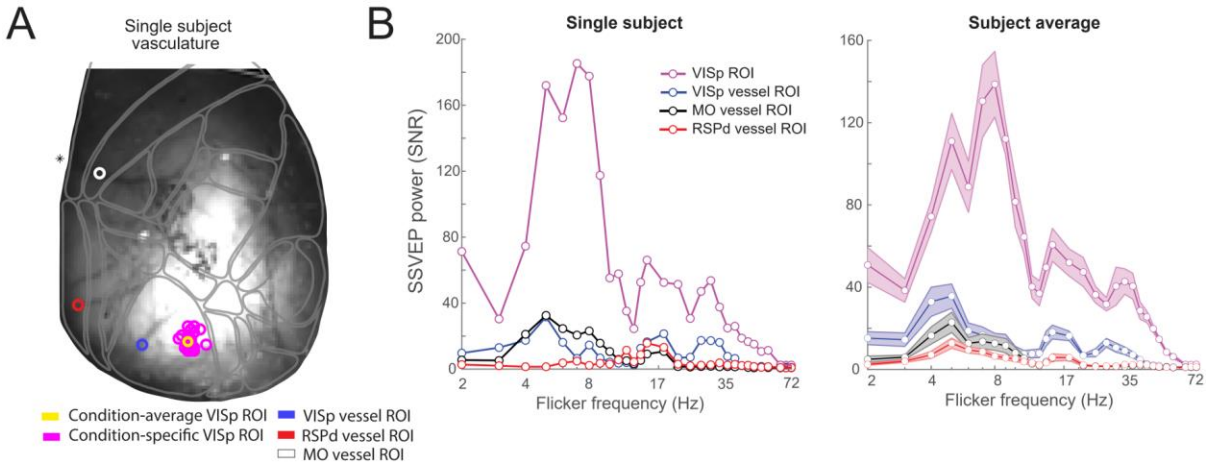

Supplementary Figure 7. Temporal frequency tuning curves from visual and non-visual ROIs positioned above blood vessels. (A) Vasculature image from a single subject used to select ROIs positioned directly over the blood vessel in retrosplenial (red circle), motor (white circle), and visual cortices (blue circle from ROI over the blood vessel in VISp, purple circles indicate flicker frequency-specific ROIs and yellow one denotes flicker condition-average ROI). (B) Temporal frequency tuning curves from a single representative subject (same as in the main text figures) and subject average. Note that only visual ROIs show resonance peaks and neither motor nor retrosplenial ROI show resonance peaks around 8 Hz, 15 Hz, or 33 Hz. A characteristic 5 Hz peak is, however, present, and again indicates a potentially non-visual nature of this rhythmic activity, which likely is a breathing rhythm as discussed in the main text and Supplementary Figure 8.

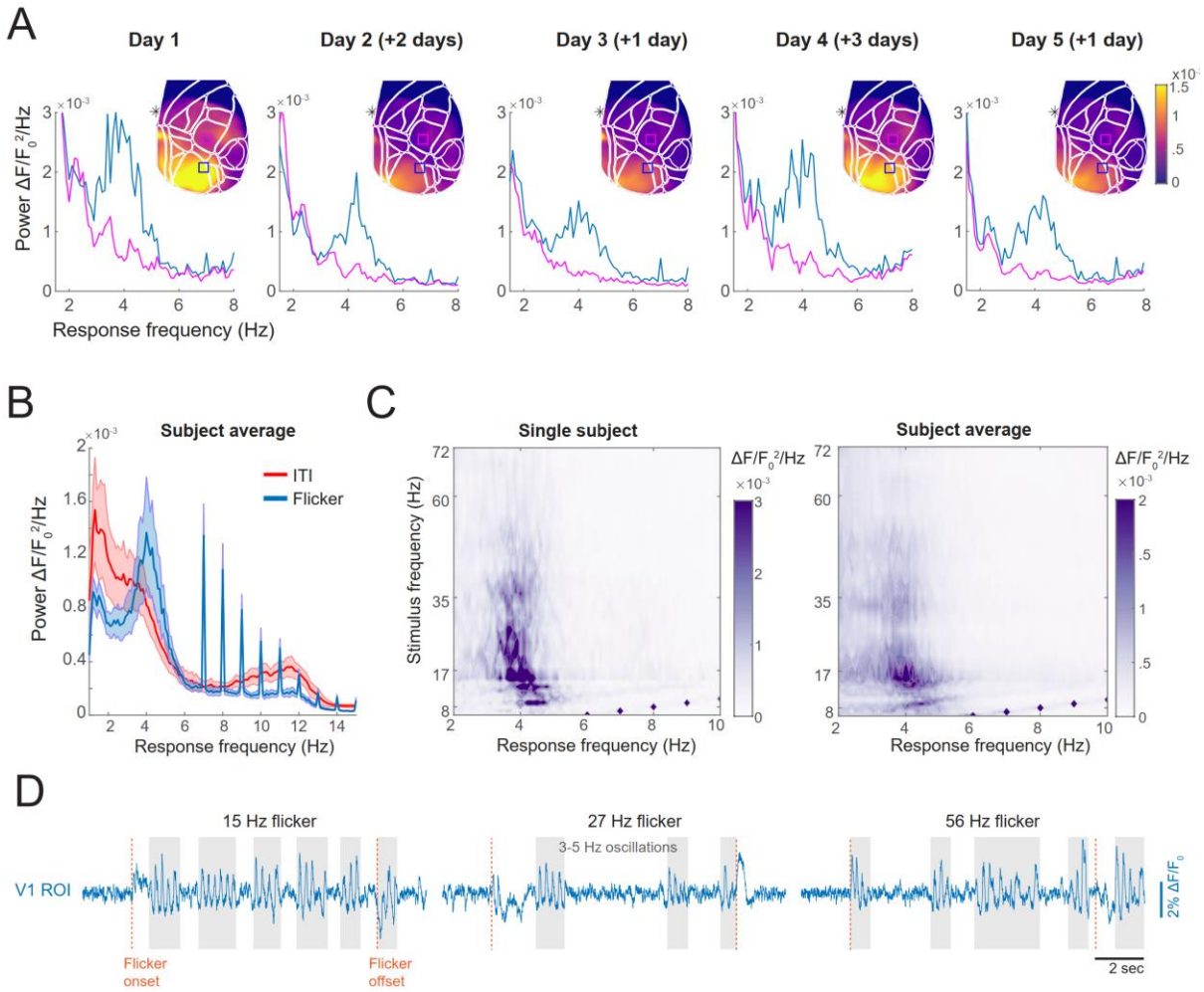

Supplementary Figure 8. Origins of 5 Hz resonance peak in temporal frequency tuning curves. (A) Power spectra from V1 ROI (blue trace) and S1 ROI (magenta trace) and topography of 3-5 Hz activity during >7 Hz flicker trials from a single animal across recording days. The 3-5 Hz activity was more prominent over visual areas (power differences between blue and magenta traces). To make sure that 3-5 Hz activity in the visual cortex was not a result of global signal regression (GSR) pre-processing step, the data plotted here does not include GSR preprocessing step. The numbers in the brackets indicate the number of days relative to the previous recording and thus the recency of exposure to the flickering stimulus. (B) 3-5 Hz rhythm was more prominent during the stimulus than during inter-trial interval (ITI). (C) The power of 3-5 Hz rhythm varied as a function of frequency, with lower flicker frequencies eliciting higher 3-5 Hz power as compared to the higher flicker frequencies. (D) Illustration of V1 ROI time series during three different flicker frequency trials (single animal data).

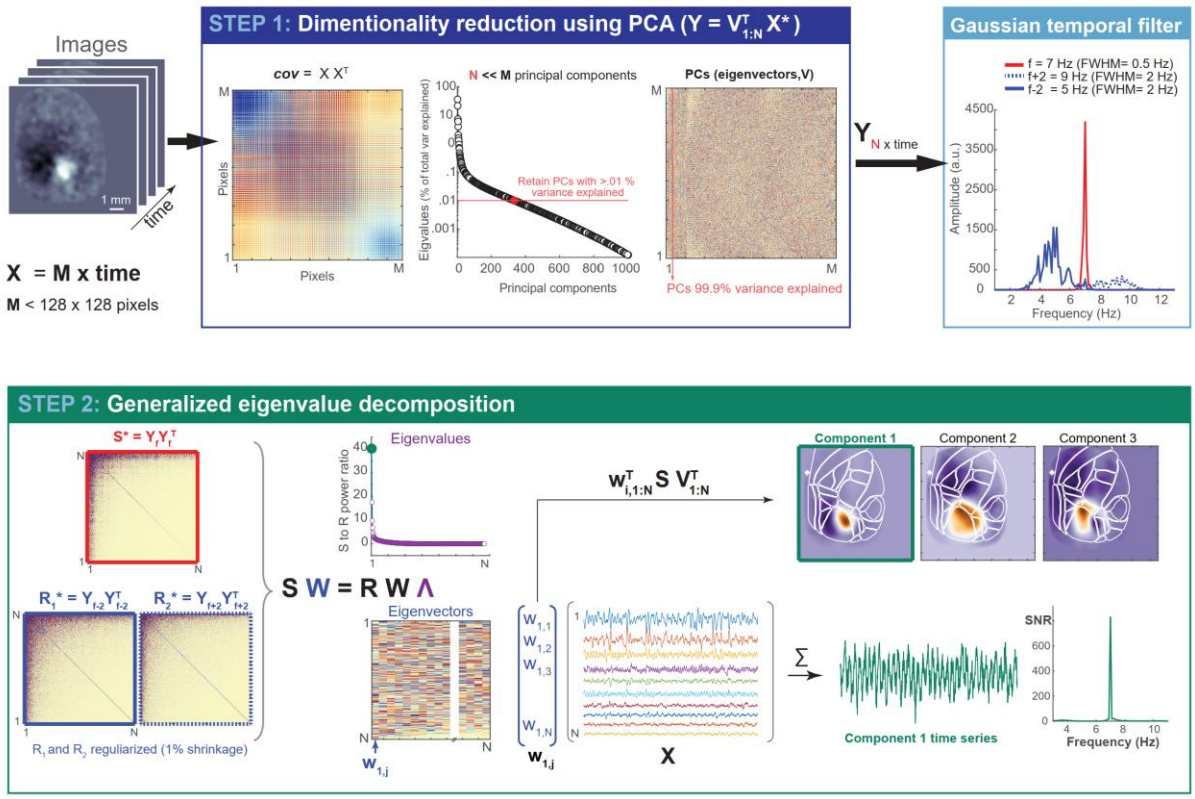

Supplementary Figure 9. Two-stage generalized eigenvalue decomposition. An illustration of analysis steps used to isolate spatiotemporal response patterns that are characteristic to a specific flicker frequency. In Step 1, a 1000-10000 ms time window of single-trial baseline-corrected fluorescence time series **X** (M x time, where M is the number of pixels containing brain data) were used to compute single-trial covariance matrices (M x M), which were averaged and submitted to PCA. Eigenvectors (principal components) associated with eigenvalues that explain more than 0.01% variance were used to reconstruct principal component time series **Y** (N x time, where N is the number of retained PCs and N << M, e.g. 364 vs. 8798). Single-trial time series **Y** were then narrow bandpass-filtered around the stimulation frequency *f* (FWHM = 0.5 Hz) and nearby frequencies $f \pm 2\ Hz$ (FWHM = 2 Hz). In Step 2, 1000-10000 ms time window of temporally filtered data was used to compute covariance matrices: signal matrix **S** (N x N) and two reference matrices **R** (N x N) that were averaged. The spatial filters that optimally separate covariance matrices **S** and **R** were computed using GED, where **W** is a matrix of eigenvectors, and **Λ** is a diagonal matrix of eigenvalues. Eigenvector $w_{i,j}$ (marked in blue in matrix **W**) associated with the highest eigenvalue λ (marked in green in diagonal of **Λ** plot) was used to reconstruct cortical maps and component time series.

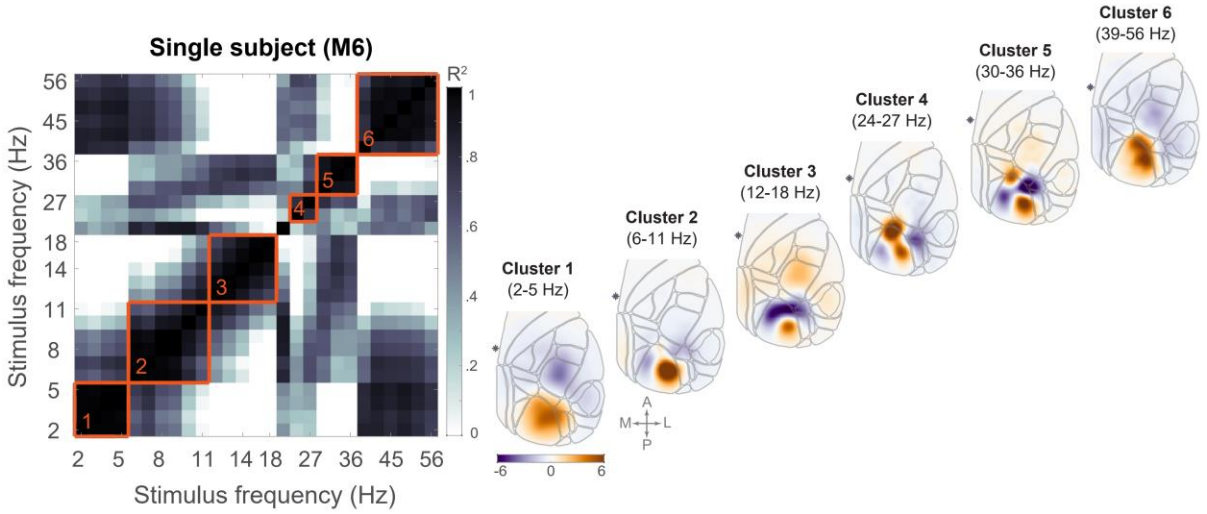

Supplementary Fig 10. Spatiotemporal resonance patters in one animal. Left: pairwise squared correlation matrix across spatiotemporal patterns generated in response to different flicker frequencies (derived using two-stage eigenvalue decomposition explained in Supplementary Figure 9). For this animal, the hierarchical clustering procedure identified 6 distinct clusters of ssVEP topographies depicted on the right. Note the similarity of cluster 4 and 5, which for other animals was identified as a single cluster.

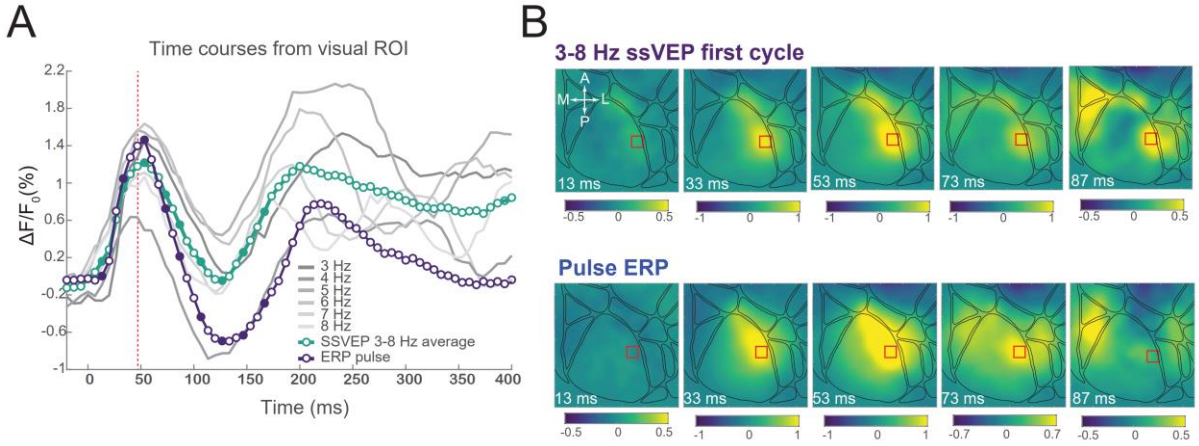

Supplementary Figure 11. Similarities of the time course between the first ssVEP cycle and pulse ERP. (A) Time courses of the first cycle of 3-8 Hz sine-wave stimulation (green trace) and pulse ERP (violet trace). Time courses are pixel-average from the ROI marked in panel B, which was defined based on the spatial peak of response in each paradigm separately. (B) Time-lapse images of stimulus-evoked activity during the first cycle of 3-8 Hz sine-wave stimulation (top row) and pulse ERP (bottom row) from the solidly colored timepoints in panel A.

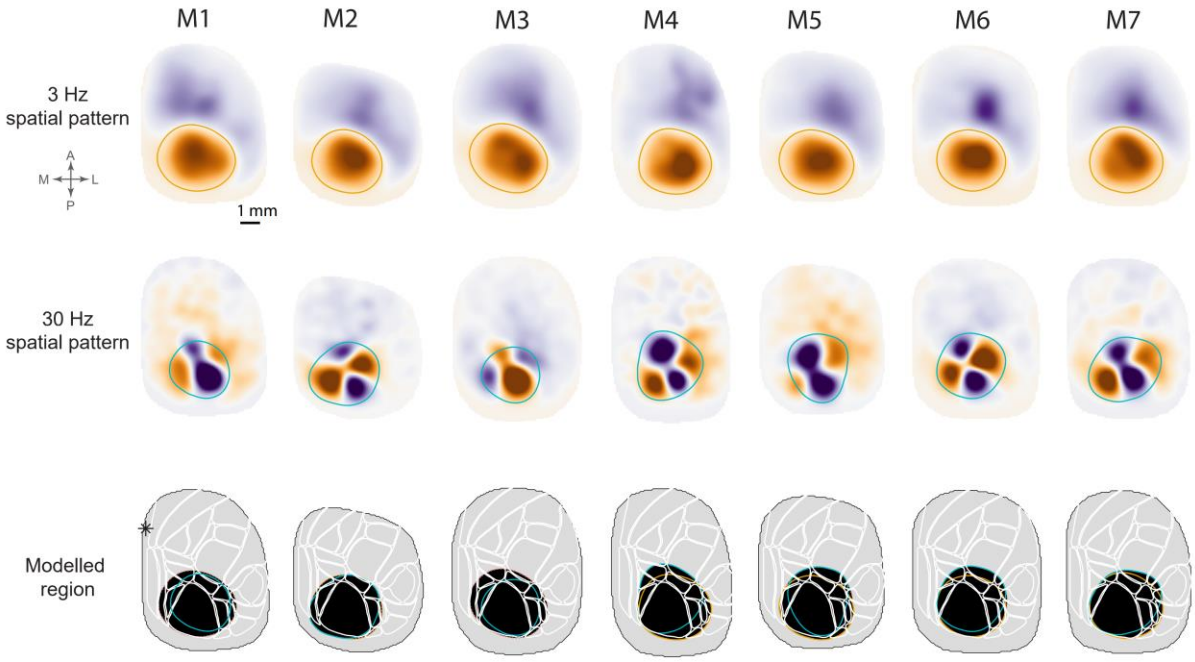

Supplementary Figure 12. Region of cortex used for modelling spatial eigenmodes. Given the clearly defined near zero amplitude contours, spatiotemporal response patterns identified using two-stage GED from two flicker conditions (3 Hz and 30 Hz) were used to define a region of posterior cortex used for modelling spatial eigenmodes. The union of regions (orange for 3 Hz condition and green for 30 Hz condition) defined from both conditions was used (black area in the bottom plots).